

MC-PDFT Nuclear Gradients and L-PDFT Energies with Meta and Hybrid Meta On-Top Functionals for Ground- and Excited-State Geometry Optimization and Vertical Excitation Energies

Matthew R. Hennefarth,¹ Younghwan Kim,¹ Bhavnesh Jangid,¹ Jacob Wardzala,¹

Matthew R. Hermes,¹ Donald G. Truhlar,^{2,*} and Laura Gagliardi^{1,3,†}

¹*Department of Chemistry and Chicago Center for Theoretical Chemistry, University of Chicago, Chicago, IL 60637, USA*

²*Department of Chemistry, Chemical Theory Center, and Minnesota Supercomputing Institute, University of Minnesota, Minneapolis, MN 55455-0431, USA*

³*Pritzker School of Molecular Engineering, University of Chicago, Chicago, IL 60637, USA*

(Dated: July 17, 2025)

Multiconfiguration pair-density functional theory (MC-PDFT) is a post-MCSCF multireference electronic-structure method that explicitly models strong electron correlation, and linearized pair-density functional theory (L-PDFT) is a recently developed multi-state extension that can accurately model conical intersections and locally-avoided crossings. Because MC-PDFT and L-PDFT rely on an on-top energy functional, their accuracy depends on the quality of the on-top functional used. Recent work has introduced translated meta-gradient-approximation (meta-GA) on-top functionals, and specifically the MC23 hybrid meta-GA on-top functional, which is the first on-top functional specifically optimized for MC-PDFT. Here we report the derivation and implementation of analytic nuclear gradients for MC-PDFT calculations using meta-GA and hybrid meta-GA on-top functionals. This development also enables analytic nuclear gradients for the widely successful tPBE0 hybrid on-top functional. Because MC-PDFT nuclear-gradient calculations involve the derivative of the on-top functional, this development also enables the use of meta-GA on-top functionals in L-PDFT single-point energy calculations. We use the new capabilities to test MC23 for ground-state geometries, excited-state geometries, and vertical excitation energies of *s-trans*-butadiene and benzophenone as well as to test MC23, another hybrid meta-GA, and seven other meta-GA on-top functionals for 441 vertical excitation energies. We find MC23 performs the best of all nine meta and hybrid meta functionals for vertical excitation energies and is comparable in accuracy to tPBE0 and to the NEVPT2 multireference wave function method. Additionally, we directly compare our MC-PDFT vertical excitation results to previously computed TD-DFT values and find that MC-PDFT outperforms even the best performing Kohn-Sham density functional.

I. INTRODUCTION

A long-standing goal of the computational chemistry community is the ability to accurately and efficiently model not only ground-state wave functions and energies of molecular systems but also the excited-state wave functions and energies. Although Kohn-Sham density functional theory (KS-DFT)¹ has excelled for a variety of computational objectives, it is a single reference method; and with currently available functionals, it is less accurate for targets with strong electron correlation – such as many electronically excited states, transition metal complexes, and bond-stretched molecules – than for systems whose electronic structure is well represented by a single Slater determinant. This motivates going beyond conventional KS-DFT to model such processes.

Active-space methods such as complete active space self-consistent field (CASSCF) theory^{2–4} or localized active space self-consistent field (LASSCF)^{5,6} theory expand the wave function in a linear combination of Slater determinants and can provide qualitatively accurate wave functions even for strongly correlated systems. However,

they are not quantitatively accurate because they fail to capture electron correlation outside the active space, which, for a good choice of active space, is mainly dynamic correlation. Multireference perturbation theories such as complete active space second-order perturbation theory (CASPT2)^{7,8} or *n*-electron valence-state second-order perturbation theory (NEVPT2)⁹ are widely employed to capture the missing electron correlation outside the active space; however, these methods are computationally expensive and can suffer from slow convergence.

Multiconfiguration pair-density functional theory (MC-PDFT)¹⁰ is an alternative post-SCF method that combines features of density functional theory with wave function theory, and it is able to capture the missing dynamic electron correlation. Starting with a multiconfiguration reference wave function, such as from CASSCF, restricted active space self-consistent field (RASSCF),^{11,12} the separated-pair approximation (SP),¹³ or LASSCF¹⁴ – MC-PDFT computes the energy using an expression that includes an on-top energy functional. Because MC-PDFT computes the energy in a one-shot manner, it generally adds no significant computational cost over the cost of calculating the reference wave function. Furthermore, it has been shown that MC-PDFT performs similarly to CASPT2¹⁵ and NEVPT2¹⁶ in predicting vertical excitation energies, and it has been success-

* corresponding author: truhlar@umn.edu

† corresponding author: lgagliardi@uchicago.edu

fully applied to study the nonadiabatic photodynamics of thioformaldehyde¹⁷ and azomethane.¹⁸

As in KS-DFT, the quality of the calculated energy is highly dependent on the choice of functional. In most work to date, MC-PDFT has used “translated”¹⁰ or “fully-translated”¹⁹ KS-DFT local-density approximation (LDA) and gradient approximation (GA) functionals. These functionals were not specifically parameterized for MC-PDFT. Recently, a translation scheme for meta-gradient-approximation (meta-GA) functionals has been devised, and the hybrid meta-GA MC23 on-top functional was introduced and parameterized for MC-PDFT ground-state energies.²⁰

Analytic nuclear gradients are necessary for geometry optimizations and direct dynamics simulations, but prior to the present work, the newly developed and optimized meta-GA functionals were implemented only for MC-PDFT energies. Here, we report the derivation and implementation of analytic nuclear gradients for meta-GA functionals and hybrid meta-GA functionals (with and without density fitting) within state-specific MC-PDFT (SS-MC-PDFT) and state-averaged MC-PDFT (SA-MC-PDFT). Our derivation and implementation also enable analytic nuclear gradients for hybrid translated LDA functionals and hybrid translated GA functionals (such as the broadly successful tPBE0²¹ functional). We first show that the analytic nuclear gradients agree with the numerical gradients for LiH. Then we demonstrate the utility of nuclear gradients in predicting ground- and excited-state geometries and adiabatic excitation energies for *s-trans*-butadiene and benzophenone.

We also consider linearized pair-density functional theory (L-PDFT),²² which is a multi-state extension of MC-PDFT that can accurately treat potential energy surfaces near conical intersections and locally-avoided crossings. L-PDFT differs from MC-PDFT in that it is more robust in modeling photochemical and photophysical processes, and it becomes computationally more efficient than MC-PDFT as the number of states within the model space grows because it only requires a single quadrature calculation regardless of the number of states within the model space. Because the L-PDFT Hamiltonian is generated from a first-order Taylor expansion of the MC-PDFT energy functional, it requires the first derivative of the on-top functional with respect to the matrix elements of the one-particle reduced density matrix (1-RDM) and two-particle reduced density matrix (2-RDM). These expressions were not previously derived for meta-GA on-top functionals, but along with the analytic nuclear gradients for MC-PDFT, we also derive the first derivative of the meta-GA on-top functionals with respect to the 1-RDM and 2-RDM, which allows us to perform L-PDFT energy calculations with meta-GA functionals. We use this new capability to report the first L-PDFT calculations using meta-GA functionals. Using the previously published QUEST wave functions,¹⁶ we benchmark both MC-PDFT and L-PDFT vertical excitation energies on the QUEST dataset^{23–28} using a variety of meta-GA on-

top functionals.

II. THEORY

Throughout this manuscript, lower-case roman letters p, q, r, s, x, y indicate general spatial molecular orbitals (MO), I and J label CASSCF eigenstates within the model space, M and N label CASSCF eigenstates in the complement of the model space (outside the model space), and κ is used for MO rotations, ξ for a general nuclear coordinate, and P for rotations between different states. Boldfaced variables are tensors (vectors, matrices, etc.). Einstein summation notation is used throughout (repeated indices are summed implicitly). Translated and fully-translated KS-DFT exchange-correlation functionals have respectively a ‘t’ or ‘ft’ prepended to their name.

A. Multiconfiguration pair-density functional theory

Until recently, the translated and fully translated on-top functionals were restricted to (pure or hybrid) translated and fully-translated LDA and GA exchange-correlation functionals.^{10,19} Recently, a translation scheme for meta-GA exchange-correlation functionals has been devised.²⁰ The resulting meta-GA on-top functionals depend on four arguments: the electron density (ρ), the gradient of the electron density ($\nabla\rho$), the kinetic energy density of the electrons (τ), and the on-top pair density (Π). We introduce the variable $\boldsymbol{\rho}$ for the collection of these four argument functions:

$$\boldsymbol{\rho} = \begin{bmatrix} \rho \\ \Pi \\ \nabla\rho \\ \tau \end{bmatrix} \quad (1)$$

The argument functions can be built from elements of the 1-RDM (γ_q^p) and 2-RDM (γ_{qs}^{pr}) as

$$\rho = \phi_p \gamma_q^p \phi^q \quad (2)$$

$$\Pi = \frac{1}{2} \phi_p \phi_r \gamma_{qs}^{pr} \phi^q \phi^s \quad (3)$$

$$\nabla\rho = (\nabla\phi_p \phi^q + \phi_p \nabla\phi^q) \gamma_q^p \quad (4)$$

$$\tau = \frac{1}{2} \nabla\phi_p \cdot \nabla\phi^q \gamma_q^p \quad (5)$$

where ϕ_p and ϕ^q are MOs.

The MC-PDFT energy for a state with these density matrices is given by^{10,20}

$$\mathcal{E}^{\text{PDFT}} = \left(h_p^q + \frac{1}{2} \mathcal{J}_p^q[\boldsymbol{\gamma}] \right) \gamma_q^p + V^{\text{nuc}} + E^{\text{ot}}[\boldsymbol{\rho}] \quad (6)$$

$$\mathcal{J}_p^q[\boldsymbol{\gamma}] = g_{pr}^{qs} \gamma_s^r \quad (7)$$

where h_p^q and g_{pr}^{qs} are the standard one- and two-electron integrals respectively, $\mathcal{J}_p^q[\boldsymbol{\gamma}]$ is the classical Coulomb interaction, V^{nuc} is the nuclear-nuclear repulsion, and E^{ot} is the on-top energy given by an integral over all space of an on-top kernel ϵ^{ot} :

$$E^{\text{ot}}[\boldsymbol{\rho}] = \int \epsilon^{\text{ot}}(\boldsymbol{\rho}(\mathbf{r})) d\mathbf{r} \quad (8)$$

In translated functionals, the arguments in $\boldsymbol{\rho}$ are translated to a set of effective spin-density variables ($\tilde{\boldsymbol{\rho}}$) that are then used to evaluate the underlying KS-DFT exchange-correlation functional.

$$\tilde{\boldsymbol{\rho}} = \begin{bmatrix} \rho_{\uparrow} \\ \rho_{\downarrow} \\ \sigma_{\uparrow\uparrow} \\ \sigma_{\uparrow\downarrow} \\ \sigma_{\downarrow\downarrow} \\ \tau_{\uparrow} \\ \tau_{\downarrow} \end{bmatrix} \quad (9)$$

For meta-GA functionals, the translation from $\boldsymbol{\rho}$ to $\tilde{\boldsymbol{\rho}}$ is defined as

$$\tilde{\boldsymbol{\rho}} = \begin{bmatrix} \frac{\rho}{2}(1 + \zeta_t) \\ \frac{\rho}{2}(1 - \zeta_t) \\ \frac{\nabla_{\rho} \cdot \nabla_{\rho}}{4} (1 + \zeta_t)^2 \\ \frac{\nabla_{\rho} \cdot \nabla_{\rho}}{4} (1 - \zeta_t)^2 \\ \frac{\nabla_{\rho} \cdot \nabla_{\rho}}{4} (1 - \zeta_t)^2 \\ \frac{\tau}{2}(1 + \zeta_t) \\ \frac{\tau}{2}(1 - \zeta_t) \end{bmatrix} \quad (10)$$

with

$$\zeta_t = \begin{cases} \sqrt{1-R} & R < 1 \\ 0 & R \geq 1 \end{cases} \quad (11)$$

and R the ratio between Π and $(\rho/2)^2$.

$$R = \frac{4\Pi}{\rho^2} \quad (12)$$

B. Linearized pair-density functional theory

L-PDFT is a multi-state extension of MC-PDFT that defines the energy operator as the first-order Taylor expansion of its MC-PDFT energy (eq. (6)) around some zeroth-order density ($\tilde{\boldsymbol{\gamma}}$).²²

$$\mathcal{E}^{\text{Lin}} = \mathcal{E}^{\text{PDFT}}[\tilde{\boldsymbol{\gamma}}] + \left. \frac{\partial \mathcal{E}^{\text{PDFT}}}{\partial \gamma_q^p} \right|_{\tilde{\boldsymbol{\gamma}}} \Delta_q^p + \left. \frac{\partial \mathcal{E}^{\text{PDFT}}}{\partial \gamma_{qs}^{pr}} \right|_{\tilde{\boldsymbol{\gamma}}} \Delta_{qs}^{pr} \quad (13)$$

$$\Delta_q^p = \gamma_q^p - \tilde{\gamma}_q^p \quad (14a)$$

$$\Delta_{qs}^{pr} = \gamma_{qs}^{pr} - \tilde{\gamma}_{qs}^{pr} \quad (14b)$$

As the L-PDFT energy is linear with respect to both the 1-RDM and the 2-RDM, it can be written as the expectation value of a quantum operator that we call the L-PDFT Hamiltonian.

$$\mathcal{E}_I^{\text{Lin}} = \langle I | \hat{H}^{\text{Lin}} | I \rangle \quad (15)$$

$$\hat{H}^{\text{Lin}} = (h_p^q + \mathcal{J}_p^q[\tilde{\boldsymbol{\gamma}}] + V_p^q[\tilde{\boldsymbol{\gamma}}]) \hat{E}_q^p + \frac{1}{2} v_{pr}^{qs}[\tilde{\boldsymbol{\gamma}}] \hat{e}_{qs}^{pr} + h^{\text{const}} \quad (16)$$

Here, \hat{E}_q^p and \hat{e}_{qs}^{pr} are respectively the singlet excitation operator and the two-electron excitation operator,²⁹ and $V_p^q[\tilde{\boldsymbol{\gamma}}]$ and $v_{pr}^{qs}[\tilde{\boldsymbol{\gamma}}]$ are the one- and two-electron on-top potential terms³⁰

$$V_p^q[\tilde{\boldsymbol{\gamma}}] = \left. \frac{\partial E^{\text{ot}}}{\partial \gamma_q^p} \right|_{\tilde{\boldsymbol{\gamma}}} \quad (17a)$$

$$v_{pr}^{qs}[\tilde{\boldsymbol{\gamma}}] = 2 \left. \frac{\partial E^{\text{ot}}}{\partial \gamma_{qs}^{pr}} \right|_{\tilde{\boldsymbol{\gamma}}} \quad (17b)$$

h^{const} is a constant term which only depends on the zeroth-order density.

$$h^{\text{const}} = V^{\text{nuc}} + E^{\text{ot}} - \left(\frac{1}{2} \mathcal{J}_p^q[\tilde{\boldsymbol{\gamma}}] + V_p^q[\tilde{\boldsymbol{\gamma}}] \right) \tilde{\gamma}_q^p - \frac{1}{2} v_{pr}^{qs}[\tilde{\boldsymbol{\gamma}}] \tilde{\gamma}_{qs}^{pr} \quad (18)$$

These equations show that the L-PDFT Hamiltonian, and thus its eigenvalues, requires the first derivative of the on-top functional with respect to the elements of the 1-RDM and 2-RDM. These were not previously derived for meta-GA functionals. Section II C derives the one- and two-electron on-top potential terms for a translated meta-GA functional which allows us to use meta-GA functionals with L-PDFT.

C. Meta-gradient-approximation one- and two-electron on-top potential terms

Both MC-PDFT nuclear gradients and L-PDFT energy calculations require the first derivative of E^{ot} with respect to the elements of the 1-RDM and 2-RDM. Moving the derivative of E^{ot} with respect to the elements of the 1-RDM and 2-RDM inside the integral of eq. (8) and applying the chain rule, we obtain

$$V_p^q = \int \mathbf{v}^{\text{ot}} \cdot \frac{\partial \rho}{\partial \gamma_q^p} d\mathbf{r} \quad (19a)$$

$$v_{pr}^{qs} = 2 \int \mathbf{v}^{\text{ot}} \cdot \frac{\partial \rho}{\partial \gamma_{qs}^{pr}} d\mathbf{r} \quad (19b)$$

where we have defined \mathbf{v}^{ot} as

$$\mathbf{v}^{\text{ot}} = \nabla_{\rho} \epsilon^{\text{ot}} \quad (20)$$

The derivatives of the collection of argument functions with respect to the elements of the 1-RDM and 2-RDM

are

$$\frac{\partial \rho}{\partial \gamma_q^p} = \begin{bmatrix} \phi_p \phi^q \\ 0 \\ \nabla \phi_p \phi^q + \phi_p \nabla \phi^q \\ \frac{1}{2} \nabla \phi_p \cdot \nabla \phi^q \end{bmatrix} \quad (21a)$$

$$\frac{\partial \rho}{\partial \gamma_{qs}^{pr}} = \begin{bmatrix} 0 \\ \frac{1}{2} \phi_p \phi_r \phi^q \phi^s \\ 0 \\ 0 \end{bmatrix} \quad (21b)$$

Because ϵ^{ot} is defined as evaluating a Kohn-Sham ϵ^{xc} with the translated effective density variables $\tilde{\rho}$, the potential \mathbf{v}^{ot} can be evaluated in terms of \mathbf{v}^{xc} :

$$\mathbf{v}^{\text{ot}} = \mathbf{v}^{\text{xc}} \cdot \mathbf{J}_{\tilde{\rho}}^{\tilde{\rho}} \quad (22)$$

where \mathbf{v}^{xc} for a meta-GA functional is defined as

$$\mathbf{v}^{\text{xc}} = \left[\frac{\partial \epsilon^{\text{xc}}}{\partial \rho_{\uparrow}} \quad \frac{\partial \epsilon^{\text{xc}}}{\partial \rho_{\downarrow}} \quad \frac{\partial \epsilon^{\text{xc}}}{\partial \sigma_{\uparrow}} \quad \frac{\partial \epsilon^{\text{xc}}}{\partial \sigma_{\downarrow}} \quad \frac{\partial \epsilon^{\text{xc}}}{\partial \tau_{\uparrow}} \quad \frac{\partial \epsilon^{\text{xc}}}{\partial \tau_{\downarrow}} \right] \quad (23)$$

and $\mathbf{J}_{\tilde{\rho}}^{\tilde{\rho}}$ is the Jacobian of the translation from ρ to $\tilde{\rho}$.

$$\mathbf{J}_{\tilde{\rho}}^{\tilde{\rho}} = \begin{bmatrix} \frac{\partial \rho_{\uparrow}}{\partial \rho} & \frac{\partial \rho_{\uparrow}}{\partial \Pi} & \frac{\partial \rho_{\uparrow}}{\partial \nabla \rho} & \frac{\partial \rho_{\uparrow}}{\partial \tau} \\ \frac{\partial \rho_{\downarrow}}{\partial \rho} & \frac{\partial \rho_{\downarrow}}{\partial \Pi} & \frac{\partial \rho_{\downarrow}}{\partial \nabla \rho} & \frac{\partial \rho_{\downarrow}}{\partial \tau} \\ \frac{\partial \sigma_{\uparrow}}{\partial \rho} & \frac{\partial \sigma_{\uparrow}}{\partial \Pi} & \frac{\partial \sigma_{\uparrow}}{\partial \nabla \rho} & \frac{\partial \sigma_{\uparrow}}{\partial \tau} \\ \frac{\partial \sigma_{\downarrow}}{\partial \rho} & \frac{\partial \sigma_{\downarrow}}{\partial \Pi} & \frac{\partial \sigma_{\downarrow}}{\partial \nabla \rho} & \frac{\partial \sigma_{\downarrow}}{\partial \tau} \\ \frac{\partial \tau_{\uparrow}}{\partial \rho} & \frac{\partial \tau_{\uparrow}}{\partial \Pi} & \frac{\partial \tau_{\uparrow}}{\partial \nabla \rho} & \frac{\partial \tau_{\uparrow}}{\partial \tau} \\ \frac{\partial \tau_{\downarrow}}{\partial \rho} & \frac{\partial \tau_{\downarrow}}{\partial \Pi} & \frac{\partial \tau_{\downarrow}}{\partial \nabla \rho} & \frac{\partial \tau_{\downarrow}}{\partial \tau} \end{bmatrix} \quad (24)$$

Although the five upper rows of the Jacobian have been derived previously,^{30,31} we include their explicit form here for completeness. We start with derivatives of ρ_{\uparrow} and ρ_{\downarrow} . Using eq. (10), it can be seen that the only nonzero derivatives of ρ_{\uparrow} and ρ_{\downarrow} are with respect to ρ and Π :

$$\frac{\partial \rho_{\uparrow}}{\partial \rho} = \frac{1 + \zeta_t}{2} - R \frac{\partial \zeta_t}{\partial R} \quad (25)$$

$$\frac{\partial \rho_{\uparrow}}{\partial \Pi} = \frac{2}{\rho} \frac{\partial \zeta_t}{\partial R} \quad (26)$$

$$\frac{\partial \rho_{\downarrow}}{\partial \rho} = \frac{1 - \zeta_t}{2} + R \frac{\partial \zeta_t}{\partial R} \quad (27)$$

$$\frac{\partial \rho_{\downarrow}}{\partial \Pi} = -\frac{2}{\rho} \frac{\partial \zeta_t}{\partial R} \quad (28)$$

where

$$\frac{\partial \zeta_t}{\partial R} = \begin{cases} \frac{-1}{2} \zeta_t^{-1} & R < 1 \\ 0 & R \geq 1 \end{cases} \quad (29)$$

Due to the stepwise form of ζ_t we do not simplify our equations further. The first derivative of σ_{ab} (where a, b can be \uparrow or \downarrow) with respect to τ is 0. The other, nonzero derivatives are given by

$$\frac{\partial \sigma_{\uparrow\uparrow}}{\partial \rho} = \frac{-|\nabla \rho|^2 R (1 + \zeta_t)}{\rho} \frac{\partial \zeta_t}{\partial R} \quad (30)$$

$$\frac{\partial \sigma_{\uparrow\uparrow}}{\partial \Pi} = \frac{2|\nabla \rho|^2 (1 + \zeta_t)}{\rho^2} \frac{\partial \zeta_t}{\partial R} \quad (31)$$

$$\frac{\partial \sigma_{\uparrow\uparrow}}{\partial \nabla \rho} = \frac{\nabla \rho}{2} (1 + \zeta_t)^2 \quad (32)$$

$$\frac{\partial \sigma_{\uparrow\downarrow}}{\partial \rho} = \frac{|\nabla \rho|^2 R \zeta_t}{\rho} \frac{\partial \zeta_t}{\partial R} \quad (33)$$

$$\frac{\partial \sigma_{\uparrow\downarrow}}{\partial \Pi} = \frac{-2|\nabla \rho|^2 \zeta_t}{\rho^2} \frac{\partial \zeta_t}{\partial R} \quad (34)$$

$$\frac{\partial \sigma_{\uparrow\downarrow}}{\partial \nabla \rho} = \frac{\nabla \rho}{2} (1 - \zeta_t^2) \quad (35)$$

$$\frac{\partial \sigma_{\downarrow\downarrow}}{\partial \rho} = \frac{|\nabla \rho|^2 R (1 - \zeta_t)}{\rho} \frac{\partial \zeta_t}{\partial R} \quad (36)$$

$$\frac{\partial \sigma_{\downarrow\downarrow}}{\partial \Pi} = \frac{-2|\nabla \rho|^2 (1 - \zeta_t)}{\rho^2} \frac{\partial \zeta_t}{\partial R} \quad (37)$$

$$\frac{\partial \sigma_{\downarrow\downarrow}}{\partial \nabla \rho} = \frac{\nabla \rho}{2} (1 - \zeta_t)^2 \quad (38)$$

Finally, since τ_{\uparrow} and τ_{\downarrow} do not depend on $\nabla \rho$, those derivatives are zero. The other non-zero derivatives are given by

$$\frac{\partial \tau_{\uparrow}}{\partial \rho} = \frac{-R\tau}{\rho} \frac{\partial \zeta_t}{\partial R} \quad (39)$$

$$\frac{\partial \tau_{\uparrow}}{\partial \Pi} = \frac{2\tau}{\rho^2} \frac{\partial \zeta_t}{\partial R} \quad (40)$$

$$\frac{\partial \tau_{\uparrow}}{\partial \tau} = \frac{1 + \zeta_t}{2} \quad (41)$$

$$\frac{\partial \tau_{\downarrow}}{\partial \rho} = \frac{R\tau}{\rho} \frac{\partial \zeta_t}{\partial R} \quad (42)$$

$$\frac{\partial \tau_{\downarrow}}{\partial \Pi} = \frac{-2\tau}{\rho^2} \frac{\partial \zeta_t}{\partial R} \quad (43)$$

$$\frac{\partial \tau_{\downarrow}}{\partial \tau} = \frac{1 - \zeta_t}{2} \quad (44)$$

Plugging eqs. (25) to (28) and (30) to (44) into eq. (24) gives the meta-GA Jacobian. The last two rows (the derivatives of τ_{\uparrow} and τ_{\downarrow} with respect to the argument functions) are the new additions in the meta-GA Jacobian.

D. Meta-gradient-approximation multiconfiguration pair-density functional theory nuclear gradients

Because neither SS-MC-PDFT³⁰ nor SA-MC-PDFT³¹ variationally optimizes the wave function variables, the analytic nuclear gradients are obtained using Lagrange's method of undetermined multipliers. As the equations for the SS-MC-PDFT nuclear gradients are a special case of the SA-MC-PDFT ones, we need to present only the more general SA-MC-PDFT nuclear gradient equations.³¹ Here we first discuss the modifications necessary in the MC-PDFT energy response terms in order to solve for the corresponding Lagrange multipliers. Then, we discuss the modifications necessary to compute the MC-PDFT Hellmann-Feynman contribution.

In general, a CASSCF wave function (state-specific or state-averaged) can be parameterized as

$$|I\rangle = e^{\hat{P}^I} e^{\hat{\kappa}} |0\rangle \quad (45)$$

where $\hat{\kappa}$ is the MO-rotation operator

$$\hat{\kappa} = \sum_{p<q} \kappa_p^q \left[\hat{\mathbf{E}} - \hat{\mathbf{E}}^\dagger \right]_q^p \quad (46)$$

and \hat{P}^I is the state-transfer operator for state $|I\rangle$. State rotations can be decomposed into rotations within the model space (\hat{P}_\parallel) and rotations out of the model space (\hat{P}_\perp).

$$\hat{P}^I = \hat{P}_\perp^I + \hat{P}_\parallel^I \quad (47)$$

$$\hat{P}_\perp^I = P_M^I (|M\rangle\langle I| - |I\rangle\langle M|) \quad (48)$$

$$\hat{P}_\parallel^I = P_J^I (|J\rangle\langle I| - |I\rangle\langle J|) \quad (49)$$

In the case of a state-specific complete active space self-consistent field theory (SS-CASSCF) wave function, $\hat{P}_\parallel^I = 0$ as the model space is spanned by a single state ($|I\rangle$).

The Lagrangian for a reference wave function $|I\rangle$ (coming from either SS-CASSCF or state-averaged complete active space self-consistent field theory (SA-CASSCF) is given by

$$\begin{aligned} \mathcal{L}_I^{\text{PDFT}} = & \mathcal{E}_I^{\text{PDFT}} + \bar{\boldsymbol{\kappa}} \cdot \nabla_{\boldsymbol{\kappa}} \mathcal{E}^{\text{SA}} + \bar{\mathbf{P}}_\perp \cdot \nabla_{\mathbf{P}_\perp} \mathcal{E}^{\text{SA}} \\ & + \omega_I \bar{\mathbf{P}}_\parallel \cdot \nabla_{\mathbf{P}_\parallel} \mathcal{E}_I^{\text{CAS}} \end{aligned} \quad (50)$$

where \mathcal{E}^{SA} is the average electronic energy within the model space, $\mathcal{E}_I^{\text{CAS}}$ is the electronic energy for state $|I\rangle$, ω_I is the weight of the I th root in the state-average, and $\bar{\boldsymbol{\kappa}}$, $\bar{\mathbf{P}}_\perp$, and $\bar{\mathbf{P}}_\parallel$ are the associated Lagrange multipliers for the MO-rotation and state-transfer operators respectively. The Lagrange multipliers $\bar{\boldsymbol{\kappa}}$, $\bar{\mathbf{P}}_\perp$, and $\bar{\mathbf{P}}_\parallel$ are determined by making $\mathcal{L}_I^{\text{PDFT}}$ stationary with respect to

MO rotations and state rotations; this requires solving the following system of coupled linear equations.

$$\begin{bmatrix} \nabla_{\boldsymbol{\kappa}} \mathcal{E}_I^{\text{PDFT}} \\ \nabla_{\mathbf{P}_\perp} \mathcal{E}_I^{\text{PDFT}} \\ \nabla_{\mathbf{P}_\parallel} \mathcal{E}_I^{\text{PDFT}} \end{bmatrix} = - \begin{bmatrix} \mathbf{H}_{\boldsymbol{\kappa}\boldsymbol{\kappa}}^{\mathcal{E}^{\text{SA}}} & \mathbf{H}_{\boldsymbol{\kappa}\mathbf{P}_\perp}^{\mathcal{E}^{\text{SA}}} & \mathbf{H}_{\boldsymbol{\kappa}\mathbf{P}_\parallel}^{\mathcal{E}^{\text{CAS}}} \\ \mathbf{H}_{\mathbf{P}_\perp\boldsymbol{\kappa}}^{\mathcal{E}^{\text{SA}}} & \mathbf{H}_{\mathbf{P}_\perp\mathbf{P}_\perp}^{\mathcal{E}^{\text{SA}}} & \mathbf{H}_{\mathbf{P}_\perp\mathbf{P}_\parallel}^{\mathcal{E}^{\text{CAS}}} \\ 0 & 0 & \mathbf{H}_{\mathbf{P}_\parallel\mathbf{P}_\parallel}^{\mathcal{E}^{\text{CAS}}} \end{bmatrix} \begin{bmatrix} \bar{\boldsymbol{\kappa}} \\ \bar{\mathbf{P}}_\perp \\ \bar{\mathbf{P}}_\parallel \end{bmatrix} \quad (51)$$

Here, $\mathbf{H}_{\mathbf{ab}}^{\mathcal{E}^{\text{SA}}}$ denotes the Hessian of \mathcal{E}^{SA} with respect to the \mathbf{a} and \mathbf{b} variables.

Because the matrix in eq. (51) is not symmetric, we cannot use the standard preconditioned conjugate gradient (PCG) method^{32,33} to solve for all of the Lagrange multipliers in a single step. Instead, we first solve for $\bar{\mathbf{P}}_\parallel$ using

$$\nabla_{\mathbf{P}_\parallel} \mathcal{E}^{\text{PDFT}} = - \mathbf{H}_{\mathbf{P}_\parallel\mathbf{P}_\parallel}^{\mathcal{E}^{\text{CAS}}} \cdot \bar{\mathbf{P}}_\parallel \quad (52)$$

Then we solve for the remaining Lagrange multipliers $\bar{\boldsymbol{\kappa}}$ and $\bar{\mathbf{P}}_\perp$ using the standard PCG method on

$$\begin{bmatrix} \nabla_{\boldsymbol{\kappa}} \mathcal{E}^{\text{PDFT}} + \mathbf{H}_{\boldsymbol{\kappa}\mathbf{P}_\parallel}^{\mathcal{E}^{\text{CAS}}} \cdot \bar{\mathbf{P}}_\parallel \\ \nabla_{\mathbf{P}_\perp} \mathcal{E}^{\text{PDFT}} + \mathbf{H}_{\mathbf{P}_\perp\mathbf{P}_\parallel}^{\mathcal{E}^{\text{CAS}}} \cdot \bar{\mathbf{P}}_\parallel \end{bmatrix} = - \begin{bmatrix} \mathbf{H}_{\boldsymbol{\kappa}\boldsymbol{\kappa}}^{\mathcal{E}^{\text{SA}}} & \mathbf{H}_{\boldsymbol{\kappa}\mathbf{P}_\perp}^{\mathcal{E}^{\text{SA}}} \\ \mathbf{H}_{\mathbf{P}_\perp\boldsymbol{\kappa}}^{\mathcal{E}^{\text{SA}}} & \mathbf{H}_{\mathbf{P}_\perp\mathbf{P}_\perp}^{\mathcal{E}^{\text{SA}}} \end{bmatrix} \begin{bmatrix} \bar{\boldsymbol{\kappa}} \\ \bar{\mathbf{P}}_\perp \end{bmatrix} \quad (53)$$

In the case of SS-MC-PDFT, there are no model-space rotations, and eq. (51) can be directly solved using the PCG method as all of the $\bar{\mathbf{P}}_\parallel$ Lagrange multipliers are zero.

The response of the MC-PDFT energy to MO rotations is known to be

$$\frac{\partial \mathcal{E}^{\text{PDFT}}}{\partial \kappa_x^y} = 2 \left[\mathcal{F}_{\text{PDFT}} - \mathcal{F}_{\text{PDFT}}^\dagger \right]_y^x \quad (54)$$

where \mathcal{F} is the MC-PDFT generalized Fock matrix.^{30,31}

$$[\mathcal{F}_{\text{PDFT}}]_y^x = (h_y^q + \mathcal{J}_y^q[\boldsymbol{\gamma}] + V_y^q[\boldsymbol{\gamma}])\gamma_q^x + v_{yr}^{qs}[\boldsymbol{\gamma}]\gamma_{qs}^{xr} \quad (55)$$

Similarly the response of the MC-PDFT energy with respect to a state rotation is known to be³¹

$$\frac{\partial \mathcal{E}_I^{\text{PDFT}}}{\partial P_\Lambda^J} = \delta_J^I \left(\langle I | \hat{H}_I^{\text{PDFT}} \hat{Q}_I | \Lambda \rangle + \langle \Lambda | \hat{Q}_I \hat{H}_I^{\text{PDFT}} | I \rangle \right) \quad (56)$$

where Λ is any configuration state function (CSF), \hat{H}_I^{PDFT} is a operator that depends on the I th state through the Coulomb and on-top potential terms, and \hat{Q}_I removes any component along the I th root.

$$\hat{H}_I^{\text{PDFT}} = (h_p^q + \mathcal{J}_p^q[\boldsymbol{\gamma}] + V_p^q[\boldsymbol{\gamma}]) \hat{E}_q^p + \frac{1}{2} v_{pr}^{qs}[\boldsymbol{\gamma}] \hat{e}_{pr}^{qs} \quad (57)$$

$$\hat{Q}_I = 1 - |I\rangle\langle I| \quad (58)$$

The eqs. (55) and (57) show that the one- and two-electron on-top potential terms for meta-GA functionals

are necessary in order to solve for the Lagrange multipliers, and section II C describes how to calculate these terms.

Having solved for the Lagrange multipliers, the nuclear gradient of $\mathcal{E}_I^{\text{PDFT}}$ is given by

$$\begin{aligned} \frac{d\mathcal{E}_I^{\text{PDFT}}}{d\xi} &= \frac{\partial \mathcal{L}_I^{\text{PDFT}}}{\partial \xi} \\ &= \frac{\partial \mathcal{E}_I^{\text{PDFT}}}{\partial \xi} + \bar{\boldsymbol{\kappa}} \cdot \nabla_{\boldsymbol{\kappa}} \frac{\partial \mathcal{E}^{\text{SA}}}{\partial \xi} + \bar{\mathbf{P}}_{\perp} \cdot \nabla_{\mathbf{P}_{\perp}} \frac{\partial \mathcal{E}^{\text{SA}}}{\partial \xi} \\ &\quad + \omega_I \bar{\mathbf{P}}_{\parallel}^I \cdot \nabla_{\mathbf{P}_{\parallel}^I} \frac{\partial \mathcal{E}_I^{\text{CAS}}}{\partial \xi} \end{aligned} \quad (59)$$

All terms except $\frac{\partial \mathcal{E}_I^{\text{PDFT}}}{\partial \xi}$, which is the MC-PDFT Hellmann-Feynman contribution, are unchanged for a meta-GA on-top functional. $\frac{\partial \mathcal{E}_I^{\text{PDFT}}}{\partial \xi}$ is given by

$$\begin{aligned} \frac{\partial \mathcal{E}_I^{\text{PDFT}}}{\partial \xi} &= \left(h_{p,\xi}^q + \mathcal{J}_{p,\xi}^q[\boldsymbol{\gamma}] \right) \gamma_q^p + V_{,\xi}^{\text{nuc}} + E_{,\xi}^{\text{ot}}[\boldsymbol{\rho}_{\boldsymbol{\gamma}}] \\ &\quad - S_{p,\xi}^q[\mathcal{F}_{\text{PDFT}}^p]_q \end{aligned} \quad (60)$$

where $h_{p,\xi}^q$ is the derivative of the one-electron integral, $\mathcal{J}_{p,\xi}^q[\boldsymbol{\gamma}]$ is the derivative of the Coulomb integral, $V_{,\xi}^{\text{nuc}}$ is the derivative of the nuclear-nuclear repulsion term, $S_{p,\xi}^q$ is the derivative of the MO overlap matrix, \mathcal{F}_q^p is the MC-PDFT generalized Fock matrix (eq. (55)), and $E_{,\xi}^{\text{ot}}[\boldsymbol{\rho}_{\boldsymbol{\gamma}}]$ is the derivative of the on-top functional. Note that the comma indicates that the tensor has been differentiated with respect to the following index.³⁴ The last term is a result of ensuring the MOs are orthonormal at all geometries and is sometimes called the ‘‘renormalization’’ or ‘‘connection’’ term. Only the nuclear derivative of the on-top functional is different for a meta-GA on-top functional. Similarly to section II C, we can move the differentiation within the integral and apply the chain-rule to find that

$$E_{,\xi}^{\text{ot}} = \int \mathbf{v}^{\text{ot}} \cdot \frac{\partial \boldsymbol{\rho}}{\partial \xi} d\mathbf{r} + \{ \epsilon^{\text{ot}} \}_{\mathbf{r} \in \mathcal{G}} \cdot \frac{\partial \mathbf{w}}{\partial \xi} \quad (61)$$

where \mathcal{G} is the set of all grid points, \mathbf{w} are the corresponding quadrature grid weights, and $\{ \epsilon^{\text{ot}} \}_{\mathbf{r} \in \mathcal{G}}$ is the vector generated by evaluating ϵ^{ot} at all grid points.

$$\{ \epsilon^{\text{ot}} \}_{\mathbf{r} \in \mathcal{G}} = [\epsilon^{\text{ot}}(\mathbf{r}_1) \quad \epsilon^{\text{ot}}(\mathbf{r}_2) \quad \dots \quad \epsilon^{\text{ot}}(\mathbf{r}_n)] \quad (62)$$

\mathbf{v}^{ot} is evaluated as described in section II C for a meta-GA on-top functional. The nuclear derivative of the collected argument functions in $\boldsymbol{\rho}$ is given by

$$\frac{\partial \boldsymbol{\rho}}{\partial \xi} = \begin{bmatrix} 2\phi_p \gamma_q^p \phi_{,\xi}^q \\ 2\phi_p \phi_r \gamma_{qs}^{pr} \phi_{,\xi}^q \phi_{,\xi}^s \\ \nabla \phi_{p,\lambda} \phi^q + \nabla \phi_p \phi_{,\xi}^q \\ \nabla \phi_{p,\xi} \cdot \nabla \phi^q \gamma_q^p \end{bmatrix} + \delta_{\xi}(\mathbf{r}) \begin{bmatrix} \nabla \rho \\ \nabla \Pi \\ \mathbf{H}_{\mathbf{r}}^{\rho} \\ \nabla \tau \end{bmatrix} \cdot \mathbf{n}_{\xi} \quad (63)$$

where $\delta_{\xi}(\mathbf{r})$ is 1 if \mathbf{r} is evaluated at a grid point associated with the atom of the coordinate ξ and is 0 otherwise; and \mathbf{n}_{ξ} is the Cartesian unit vector for the coordinate direction ξ . Finally, $\nabla \tau$ is given by

$$\nabla \tau = \nabla \phi^q \cdot \mathbf{H}_{\mathbf{r}}^{\phi^p} \gamma_q^p \quad (64)$$

with $\mathbf{H}_{\mathbf{r}}^{\phi^p}$ being the Hessian of the p th MO with respect to the electron coordinate \mathbf{r} .

E. Hybrid multiconfiguration pair-density functional theory nuclear gradients

MC-PDFT with a hybrid functional is defined as a weighted average of the CASSCF and non-hybrid MC-PDFT energy where λ controls the fraction of CASSCF energy included.²¹

$$\mathcal{E}^{\text{Hyb}} = \lambda \mathcal{E}^{\text{CAS}} + (1 - \lambda) \mathcal{E}^{\text{PDFT}} \quad (65)$$

For example, the tPBE0 functional sets $\lambda = 0.25$, and the MC23 functional sets $\lambda = 0.2856$. The resulting hybrid MC-PDFT Lagrangian is

$$\begin{aligned} \mathcal{L}_I^{\text{Hyb}} &= \mathcal{E}_I^{\text{Hyb}} + \bar{\boldsymbol{\kappa}} \cdot \nabla_{\boldsymbol{\kappa}} \mathcal{E}^{\text{SA}} + \bar{\mathbf{P}}_{\perp} \cdot \nabla_{\mathbf{P}_{\perp}} \mathcal{E}^{\text{SA}} \\ &\quad + \omega_I \bar{\mathbf{P}}_{\parallel}^I \cdot \nabla_{\mathbf{P}_{\parallel}^I} \mathcal{E}_I^{\text{CAS}} \end{aligned} \quad (66)$$

We solve for the Lagrange multipliers in the same way as for the non-hybrid functional (eqs. (51) to (53)). For SS-MC-PDFT, the CASSCF energy is stationary with respect to MO and state rotations which allows for a further simplification where the non-hybrid SS-MC-PDFT Lagrange multipliers are just scaled by $1 - \lambda$. However, in the general SA-MC-PDFT, it requires modified MC-PDFT energy response terms. The resulting hybrid energy response to MO rotations is given by

$$\frac{\partial \mathcal{E}^{\text{Hyb}}}{\partial \kappa_x^y} = 2 \left[\mathcal{F}_{\text{Hyb}} - \mathcal{F}_{\text{Hyb}}^{\dagger} \right]_y^x \quad (67)$$

$$\mathcal{F}_{\text{Hyb}} = \lambda \mathcal{F}_{\text{CAS}} + (1 - \lambda) \mathcal{F}_{\text{PDFT}} \quad (68)$$

where \mathcal{F}_{CAS} is the CASSCF generalized Fock matrix.

$$[\mathcal{F}_{\text{CAS}}]_y^x = h_y^q \gamma_q^x + g_{yr}^{qs} \gamma_{qs}^{xy} \quad (69)$$

Similarly, the response of the hybrid energy to a state rotation is given by

$$\frac{\partial \mathcal{E}_I^{\text{Hyb}}}{\partial P_{\Lambda}^J} = \delta_J^I \left(\langle I | \hat{H}_I^{\text{Hyb}} \hat{Q}_I | \Lambda \rangle + \langle \Lambda | \hat{Q}_I \hat{H}_I^{\text{Hyb}} | I \rangle \right) \quad (70)$$

$$\hat{H}_I^{\text{Hyb}} = \lambda \hat{H}^{\text{el}} + (1 - \lambda) \hat{H}_I^{\text{PDFT}} \quad (71)$$

where \hat{H}^{el} is the normal electronic Hamiltonian.

$$\hat{H}^{\text{el}} = h_p^q \hat{E}_q^p + \frac{1}{2} g_{pr}^{qs} \hat{e}_{pr}^{qs} + V^{\text{nuc}} \quad (72)$$

Furthermore, once the Lagrange multipliers have been obtained, the MC-PDFT Hellmann-Feynman contribution must be modified as

$$\frac{\partial \mathcal{E}^{\text{Hyb}}}{\partial \xi} = \lambda \frac{\partial \mathcal{E}^{\text{CAS}}}{\partial \xi} + (1 - \lambda) \frac{\partial \mathcal{E}^{\text{PDFT}}}{\partial \xi} \quad (73)$$

with $\frac{\partial \mathcal{E}^{\text{CAS}}}{\partial \xi}$ the normal CASSCF Hellmann-Feynman contribution.

$$\frac{\partial \mathcal{E}^{\text{CAS}}}{\partial \xi} = h_{p,\xi}^q \gamma_q^p + \frac{1}{2} g_{pr,\xi}^{qs} \gamma_{qs}^{pr} + V_{,\xi}^{\text{nuc}} - S_{p,\xi}^q [\mathcal{F}_{\text{CAS}}]_q^p \quad (74)$$

F. Meta-gradient-approximation and hybrid nuclear gradients with density fitting

One of the major bottlenecks in an energy and gradient calculation is computing the four-index electron-repulsion integrals and transforming them from the atomic orbital (AO) basis to the MO basis as this scales as $\mathcal{O}(N_{\text{basis}}^5)$ with N_{basis} the number of basis functions. Density fitting procedures – also known as the resolution of identity – such as the Cholesky decomposition,³⁵ can reduce this scaling by one to two orders of magnitude and are an invaluable technique for practical calculations. Because MC-PDFT density fitting is currently used for the electron-repulsion integrals and not for the two-electron on-top potential terms,³⁶ no modifications are necessary to the nuclear gradients for meta-GA or hybrid on-top functionals.

III. COMPUTATIONAL METHODS

All calculations were performed using PYSCF (version 2.8.0)^{37,38} and PYSCF-FORGE (version 1.0.3, commit 400b3b6)³⁹ compiled with LIBCINT (version 6.1.1)⁴⁰ and LIBXC (version 7.0.0).^{41,42} MC-PDFT meta-GA nuclear gradients and L-PDFT meta-GA single-point energy calculations are implemented in PYSCF-FORGE, which is available at <https://github.com/pyscf/pyscf-forge>.

To validate the analytic gradients, we compared them to numerical gradients for the LiH molecule using the aug-cc-pVTZ basis set^{43,44} and a (2e, 2o) active space comprising the σ and σ^* orbitals. Calculations were performed both for the ground state using state-specific methods and for the lowest two singlet states using state-averaged methods. All calculations employed the `csf_solver` from MRH (commit a88c476d).⁴⁵ A quadrature grid level of 6 was used, corresponding to 80 or 120 radial points and 770 or 974 angular points for atoms in periods 1 or 2, respectively. Both the hybrid GA functional tPBE0²¹ and the hybrid meta-GA functional MC23²⁰ were used.

Geometry optimizations for *s-trans*-butadiene and benzophenone were performed using GEOMETRIC (version 1.0)⁴⁶ with a quadrature grid level of 6. For *s-trans*-butadiene, we used the jul-cc-pVTZ basis set^{43,44,47–49}

with a (4e, 4o) active space, consisting of the 2π and $2\pi^*$ orbitals, and we included two 1A_g states in the state-averaged manifold. For benzophenone, we used the cc-pVDZ basis set⁴³ with an (8e, 7o) active space consisting of the $n_O, 2(\pi, \pi^*), \pi_{CO}$, and π_{CO}^* orbitals (fig. 1) with two 1A states and one 1B state in the state-averaged manifold. We performed the *s-trans*-butadiene calculations by imposing C_{2h} symmetry and the benzophenone calculations with C_2 symmetry. Density fitting³⁶ was employed in the benzophenone calculations.

Nine meta-GA and hybrid meta-GA functionals were tested for vertical excitations with MC-PDFT and L-PDFT. The tested functionals are

- MC23²⁰
- translated TPSS^{50,51} (tTPSS)
- translated TPSSh⁵² (tTPSSh, defined as the hybrid, meta-GA on-top functional of the translated TPSS exchange-correlation functional with λ set to 0.10 in eq. (65))
- translated SCAN⁵³ (tSCAN)
- translated r²SCAN^{54,55} (tr²SCAN)
- translated M06-L⁵⁶ (tM06-L)
- translated revM06-L⁵⁷ (trevM06-L)
- translated MN15-L⁵⁸ (tMN15-L)
- translated τ -HCTH⁵⁹ (t τ -HCTH).

Note that MC23 is a hybrid translated meta-generalized-gradient-approximation (meta-GGA) (a special case of meta-GA), tMN5-L is a translated meta-nonseparable-gradient-approximation (another special case of meta-GA), tTPSSh is a hybrid translated meta-GGA, and the other six are (non-hybrid) translated meta-GGAs.

For benchmarking these functionals, we used SACASSCF wave functions published in our previous study,¹⁶ where the approximate pair coefficient scheme⁶⁰ was applied to select the active space. Specifically, we used the “Aug(12,12)” wave functions, which are constructed with the aug-cc-pVTZ basis set^{43,44} and where, as explained in more detail in the previous paper,¹⁶ “(12,12)” means that the an active space has fewer configurations than a (12e, 12o) active space.

The accurate results used for benchmarking are the QUEST database that contains theoretical best estimate (TBE) energies of 542 vertical excitations of main-group molecules containing up to 10 non-hydrogen atoms.^{24–28} The NEVPT2 results are from strongly contracted NEVPT2.⁹

TABLE I. Mean signed error (MSE), mean unsigned error (MUE), and root-mean-squared error (RMSE) of the analytic gradients (in hartree/bohr) relative to the numerical gradients for LiH

Functional	State-Specific		State-Averaged	
	tPBE0	MC23	tPBE0	MC23
MSE	7.5×10^{-7}	-2.2×10^{-6}	2.6×10^{-6}	2.8×10^{-6}
MUE	4.1×10^{-6}	6.1×10^{-6}	6.6×10^{-6}	6.7×10^{-6}
RMSE	7.4×10^{-6}	1.0×10^{-5}	9.4×10^{-6}	1.0×10^{-5}

IV. RESULTS AND DISCUSSION

A. Numerical validation of nuclear gradients

We first verify our implementation of MC-PDFT analytic nuclear gradients with a SS-CASSCF and SA-CASSCF reference wave functions using a hybrid GA (tPBE0) and a hybrid meta-GA (MC23) functional by comparing the analytic and numerical nuclear gradients for the diatomic system LiH as functions of the Li–H bond distance. We calculated the numerical nuclear gradients using the central-difference method with a step size of δ .

$$\text{Num}(\delta) = \frac{\mathcal{E}^{\text{PDFT}}(\lambda + \delta) - \mathcal{E}^{\text{PDFT}}(\lambda - \delta)}{2\delta} \quad (75)$$

This method has an error of $\mathcal{O}(\delta^2)$; and since it depends explicitly on the step-size δ , we extrapolate to the $\delta \rightarrow 0$ limit by taking a sequence of numerical gradients with different δ values and performing a linear regression on the plot of numerical gradient versus δ^2 . The y -intercept from this regression is taken to be the best estimate of the numerical gradient.

Because both the analytic and numerical gradients depend on a wave function that can only be converged to a finite precision, there is inherent error in both values. Regardless, consistently with our prior work,^{30,31,61,62} we refer to the numerical value as the reference for the rest of the manuscript.

Table I summarizes the statistical agreement between the analytic and numerical gradients for LiH using SS-MC-PDFT or SA-MC-PDFT. SS-MC-PDFT has a mean unsigned error (MUE) of 4.1×10^{-6} hartree/bohr for the tPBE0 functional and 6.1×10^{-6} hartree/bohr for the MC23 functional. SA-MC-PDFT has MUEs of 6.6×10^{-6} hartree/bohr and 6.7×10^{-6} hartree/bohr for the tPBE0 and MC23 functionals respectively. For all cases, the MUE is on the order of 1×10^{-6} hartree/bohr, which is consistent with the agreement between the analytic and numerical nuclear gradients from our prior work.^{31,61,62} See section S1 and fig. S1-S4 for a detailed comparison of the analytical and nuclear gradients.

Overall, we find good agreement between the analytic and numerical gradients for LiH using either a translated hybrid GA or hybrid meta-GA on-top functional with either SS-MC-PDFT or SA-MC-PDFT.

B. The *s-trans*-butadiene molecule

The *s-trans*-butadiene molecule is known to have significant multireference character in both its ground and excited 1A_g states,⁶³ and we use its ground- and excited-state geometries as our first optimization tests. Table II presents the optimized and reference values for the key internal coordinates of the 1^1A_g and 2^1A_g states of *s-trans*-butadiene computed with various on-top functionals. We use a (4e, 4o) active space consisting of 2π and $2\pi^*$ orbitals. For the ground-state geometry reference, we take the experimental values from Haugen *et al.*⁶⁴, and for the excited-state reference, we take our prior SA(2)-CASPT2(4,4) calculation.³¹ We also include ground-state results from third-order coupled cluster (CC3) theory.²³

Table II shows that the internal coordinates of both the ground- and excited-state geometries of *s-trans*-butadiene show minimal variation when switching between the tPBE and tPBE0 on-top functionals. In most cases, as might be expected, the tPBE0 results fall between those obtained with tPBE and SA-CASSCF. For the excited-state geometry, the MC23 functional yields coordinates closest to the CASPT2 reference among all the PDFT methods, which is encouraging because MC23 was optimized solely for ground-state properties and a few spin splittings. It is satisfying that *all* on-top functionals produce similar geometries, with no significant deviations observed for either state.

Table III compares the vertical and adiabatic excitation energies computed with various on-top functionals to various other high-level electronic-structure results, including TBEs. There are two very-high-quality TBEs for the vertical excitation energy of *s-trans*-butadiene in the literature. Watson and Chan⁶⁵ estimate the vertical excitation energy to be 6.39 eV using extrapolated equation of motion coupled cluster calculations and Loos *et al.*²³ estimate the vertical excitation energy to be 6.50 eV using extrapolated complete-basis-set full configuration interaction (FCI) calculations. They are both designated as TBE in table III since it is not certain which is more accurate. Both multi-state complete active space second-order perturbation theory (MS-CASPT2) (at the experimental geometry)⁶³ and CASPT2³¹ perform similarly for the vertical excitation energy, differing by only 0.01 eV. Similarly, L-tPBE and tPBE differ by only 0.01 eV, showing that state interaction between the 1^1A_g and 2^1A_g states is not important for this excitation (state interaction between closely spaced excited states is usually more important than state interaction between an excited state and the ground state). This also illustrates how the multistate L-PDFT does not degrade the accuracy of single-state MC-PDFT in a case where the states coupled do not interact strongly. The table shows that tPBE0 performs the best of all of the PDFT methods at predicting the vertical excitation energy.

For the adiabatic excitation energy, we take our prior CASPT2 results as our reference.³¹ MC23 performs al-

TABLE II. Selected optimized internal coordinates (in Å and degrees) for the ground and excited 1A_g states of *s-trans*-butadiene

Method	Basis Set	$1\ ^1A_g$			$2\ ^1A_g$		
		$r_{C=C}$	r_{CC}	θ_{CCC}	$r_{C=C}$	r_{CC}	θ_{CCC}
Pair-density functional theory							
SA(2)-tPBE(4,4)	jul-cc-pVTZ	1.336	1.459	124.1	1.497	1.398	124.1
SA(2)-tPBE0(4,4)	jul-cc-pVTZ	1.338	1.458	124.2	1.497	1.402	123.9
SA(2)-MC23(4,4)	jul-cc-pVTZ	1.335	1.451	123.8	1.491	1.397	123.3
L(2)-tPBE(4,4) ⁶²	jul-cc-pVTZ	1.335	1.460	124.1	1.496	1.399	124.1
Comparison results							
SA(2)-CASSCF(4,4)	jul-cc-pVTZ	1.345	1.456	124.3	1.497	1.413	123.2
SA(2)-CASPT2(4,4) ³¹	aug-cc-pVTZ	1.342	1.454	123.6	1.488	1.394	122.1
CC3 ²³	aug-cc-pVTZ	1.340	1.453	123.9			
exp. ⁶⁴		1.343	1.467	122.8			

 TABLE III. Adiabatic and vertical excitations energies in eV (not including vibrational energy) for the $1\ ^1A_g \rightarrow 2\ ^1A_g$ excitation of *s-trans*-butadiene

Method	Basis Set	Vertical	Adiabatic
Pair-density functional theory			
SA(2)-tPBE(4,4)	jul-cc-pVTZ	6.91	5.77
SA(2)-tPBE0(4,4)	jul-cc-pVTZ	6.82	5.68
SA(2)-MC23(4,4)	jul-cc-pVTZ	6.91	5.78
L(2)-tPBE(4,4) ⁶²	jul-cc-pVTZ	6.92	5.78
Comparison results			
SA(2)-CASSCF(4,4)	jul-cc-pVTZ	6.56	5.42
SA(2)-CASPT2(4,4) ³¹	aug-cc-pVTZ	6.68	5.68 ^b
MS(2)-CASPT2(4,4) ^{a,63}	6-31G**	6.69	
CCSD ^{a,63}	6-31G**	7.69	
CC3 ²³	aug-cc-pVTZ	6.67	
Watson and Chan ⁶⁵		6.39 ^b	
Loos <i>et al.</i> ²³		6.50 ^b	

^a Excitation energy calculated at experimental equilibrium geometry

^b Theoretical best estimate

most identically to tPBE for both the vertical and adiabatic excitation. Similarly, tPBE0 gives an adiabatic excitation energy identical to that of CASPT2, making it the best performing on-top functional for predicting the *s-trans*-butadiene excitation energies.

C. Benzophenone

Next we discuss the ground- and first-singlet excited-state geometry of benzophenone (fig. 1). Benzophenone is an important triplet photosensitizer and is a prototype for the photochemistry of more complex aromatic ketones. It is known that transitions from the S_1 state to the triplet manifold proceed with near-unit quantum yield in single crystals, solutions, and isolated matrices.^{66–68} Benzophenone has been studied extensively both experimentally and computationally.

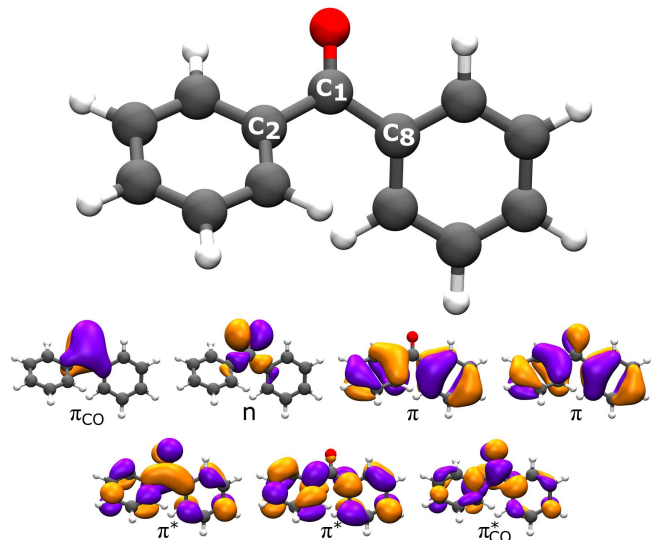


FIG. 1. Ground-state geometry of benzophenone optimized with SA(3)-tPBE(8,7), and the orbitals in the (8e,7o) active space.

It is known that the ground- and first-singlet excited-state geometries have C_2 symmetry. There is a balance between conjugation and steric effects between the two phenyl rings. The conjugation favors coplanarity whereas the steric effects between the phenyl hydrogen's favors breaking the coplanarity. The S_0 to S_1 geometry change is characterized by an elongation of the C=O bond and a reduction of the angle between the phenyl rings (which we denote as τ).^{69,70}

We use an (8e, 7o) active space comprising an oxygen nonbonding orbital, the C=O π and π^* orbitals, and 2π and $2\pi^*$ orbitals on each of the phenyl groups (fig. 1). The first singlet excitation is of $n \rightarrow \pi^*$ character with both the ground- and excited-state wave functions having 1A symmetry. Table IV summarizes selected optimized internal coordinates for these two 1A states. For the

TABLE IV. Selected optimized internal coordinates for the ground and excited 1^1A states of benzophenone^a

Method	1^1A				2^1A			
	$r_{C=O}$	$r_{C_1C_2}$	$\theta_{C_2C_1C_8}$	τ	$r_{C=O}$	$r_{C_1C_2}$	$\theta_{C_2C_1C_8}$	τ
SA(3)-CASSCF	1.213	1.501	121.2	58.5	1.369	1.445	130.9	38.8
SA(3)-tPBE	1.218	1.514	119.7	55.6	1.353	1.444	129.9	37.8
SA(3)-tPBE0	1.217	1.510	120.1	56.4	1.358	1.444	130.2	38.0
SA(3)-MC23	1.216	1.502	119.9	54.5	1.355	1.437	130.1	37.4
XMS(3)-CASPT2 ⁷¹	1.231	1.500	119.1	52.9	1.350	1.444	128.6	39.4
exp. ⁷²	1.231	1.496	121.7	55.5				

^a Atoms are numbered according to fig. 1. All bond lengths are in Å and all angles are in degrees. τ is defined as the angle between the two planes of the phenyl rings. All calculations in this table use an (8e,7o) active space and the cc-pVDZ basis set.

ground-state geometry we take the experimental structure from Fleischer *et al.*⁷² as our reference, and for the excited-state geometry we take the extended multi-state complete active space second-order perturbation theory (XMS-CASPT2) structure⁷¹ as our reference.

For the ground state, table IV shows that SA-CASSCF and all of the PDFPT methods underestimate the C=O bond length whereas XMS-CASPT2 agrees with the experimental value of 1.231 Å. For the C₁–C₂ bond, MC23 and XMS-CASPT2 get bond length close to the experimental one. For the C₂–C₁–C₈ bond angle, SA-CASSCF gets the closest to the experimental quantity followed by tPBE0. For the angle between the two phenyl rings (τ), MC23 gets the closest to the experimental 55.5°.

For the excited-state geometry, table IV shows that SA-CASSCF significantly overestimates the C=O bond length, and all three PDFPT methods reduce the error by more than a factor of two, with tPBE getting closest to the XMS-CASPT2 bond length. For the C₁–C₂ bond length, both tPBE and tPBE0 agree within 0.001 Å with XMS-CASPT2, whereas MC23 predicts a slightly shorter bond length by 0.007 Å. The SA-CASSCF method, tPBE, and tPBE0 predict that the angle between the phenyl rings is smaller in the excited-state than in the ground state by 18° to 20°, MC23 predicts it is smaller by 117°, and XMS-CASPT2 predicts it is smaller by 13.5°. In summary, there are no large deviations between any of the on-top functionals in predicting the ground- and excited-state structures of benzophenone with all methods in general agreement with both the experimental value and XMS-CASPT2.

Table V summarizes the adiabatic and vertical excitation energies of benzophenone as calculated with various on-top functionals. An experimental quantity from Itoh⁷³ suggests that the vertical excitation energy is 3.61 eV, which CASPT2 with a larger (12e, 11o) and (16e, 15o) active space (both calculated at the SA-CASSCF optimized geometry) gets to within 0.05 eV of.⁷⁰ Both tPBE and tPBE0 predict a vertical excitation of 3.78 eV with an error of 0.17 eV relative to the experimental value. A prior calculation using coupled cluster singles doubles (CCSD) predicts an even higher excitation with an error of 0.39 eV, worse than SA-CASSCF.

TABLE V. Adiabatic and vertical excitation energies in eV (not including vibrational zero-point energy) for the $1^1A \rightarrow 2^1A$ excitation of benzophenone

Method	Basis set	Vertical	Adiabatic
SA(3)-CASSCF(8,7)	cc-pVDZ	3.83	3.04
SA(3)-tPBE(8,7)	cc-pVDZ	3.78	3.25
SA(3)-tPBE0(8,7)	cc-pVDZ	3.78	3.19
SA(3)-MC23(8,7)	cc-pVDZ	3.82	3.22
SA(4)-CASPT2(12,11) ^{a,70}	ANO-L-VDZP	3.64	3.15
SA(4)-CASPT2(16,15) ^{a,70}	ANO-L-VDZP	3.66	
XMS(3)-CASPT2(8,7) ⁷¹	cc-pVDZ		3.36
CCSD ^{a,70}	cc-pVDZ	4.00	
exp. ⁷³		3.61	

^a Excitation energy calculated at SA(4)-CASSCF(12/11)/ANO-L-VDZP optimized geometries.

For the adiabatic excitation, we take the XMS-CASPT2 as our reference value. All PDFPT calculations lie between the XMS-CASPT2 and CASPT2 results. tPBE gets the closest to the XMS-CASPT2 result, followed by MC23. The performance of tPBE0 is hampered due to SA-CASSCF predicting a lower adiabatic excitation energy, with a deviation of 0.32 eV relative to the XMS-CASPT2 value.

D. Performance of meta-gradient-approximation functionals in predicting vertical excitation energies in the QUEST database

Here, we study meta-GA functionals with MC-PDFT and L-PDFT for the prediction of vertical excitation energies in a dataset of 441 excitations for which accurate results are available in the QUEST database,^{23–28} and reference SA-CASSCF wave functions are available from a previous study.¹⁶ Excitations for which a tPBE0 excitation energy calculated with these available SA-CASSCF reference wave functions has an unsigned deviation from the reference value greater than 0.55 eV have been removed from the original set of 520 excitations (giving the subset of 441 excitations) because that may be an indication that the active spaces of those reference wave functions are inadequate. In this way, we are testing

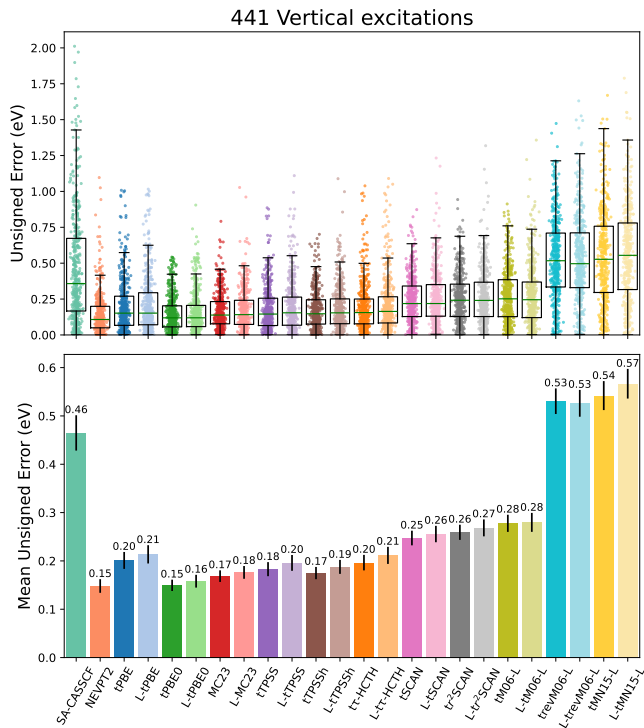


FIG. 2. Error statistics across the 441 excitations for SA-CASSCF, NEVPT2, and 11 functionals for MC-PDFT and L-PDFT. Top: Distribution of vertical excitation UE and box and whisker plots. Each dot represents a single UE for the given method. The box represents the inter-quartile range and the horizontal green lines within each box indicates the median value. The whiskers extend out 1.5 times the inter-quartile range. Bottom: Bar plots of the MUE for each method on the 441 excitations with the black vertical lines indicating the 95 % confidence intervals. SA-CASSCF, tPBE, tPBE0, and NEVPT2 data are taken from King *et al.*¹⁶; and L-tPBE and L-tPBE0 data are taken from Hennefarth *et al.*⁷⁴

only with SA-CASSCF wave functions that should be adequate. The distribution of unsigned error (UE) and MUE for the 441 retained excitations are shown in fig. 2. A plot for the entire 540 excitations is shown in fig. S5 in the supporting information.

We study one translated GA (tPBE), one hybrid translated GA (tPBE0), seven translated meta-GAs (tTPSS, t τ -HCTH, tSCAN, t τ^2 SCAN, tM06-L, trevM06-L, and tMN15-L) and two hybrid meta-GAs (tTPSSh and MC23). Figure 2 shows that tPBE0 (with an MUE of 0.15 eV) exhibits the best overall performance, matching that of NEVPT2 (MUE 0.15 eV) for the subset selected by the tPBE0 error threshold, and fig. S5 shows that it also performs best for the entire data set without filtering, although in that case the MUE of 0.44 eV is much higher. Among the tested translated meta-GA and hybrid translated meta-GA functionals, MC23 shows the best performance (MUE 0.17 eV), followed by tTPSS (0.18 eV), tTPSSh (0.18 eV eV), t τ -HCTH (0.20 eV), tSCAN (0.25 eV), t τ^2 SCAN (0.26 eV), tM06-L (0.28 eV),

trevM06-L (0.53 eV), and tMN15-L (0.54 eV).

Comparisons between L-PDFT and MC-PDFT results for each functional reveal a strong correspondence, with a difference in MUEs generally within 0.02 eV. While fig. 2 might suggest that L-PDFT performs consistently worse (by 0.01 eV) than MC-PDFT across all functionals, this is a consequence of the thresholding based on the tPBE0 error. When thresholding is performed using the L-tPBE0 error, the trend is reversed: L-PDFT shows equal or improved accuracy for most functionals (fig. S6). These results indicate that L-PDFT successfully reproduces MC-PDFT performance within the scope of this benchmark and can be routinely applied to study excitations. The findings are consistent with our previous study, where tPBE and tPBE0 were tested.⁷⁴

E. Comparing MC-PDFT to KS-DFT

We also compare the performance of MC-PDFT to the performance of time-dependent density functional theory (TD-DFT) as studied by Liang *et al.*⁷⁵, who tested more than 40 KS-DFT functionals on a 463-excitation subset of QUESTDB. Due to differing selection criteria, the subsets used in our study and theirs are not identical. Therefore, we focus on the intersection of the two data sets, which comprises 359 excitations (listed in supporting information SIII); this enables a direct comparison between the two benchmark studies. The distributions of UEs and MUEs for each study’s best-performing methods are shown in fig. 3, while the MUEs of all methods tested in our study and in Liang *et al.*⁷⁵ are shown in table S1 and S2, respectively. The best performing KS-DFT functional is M06-SX⁷⁶ with an MUE of 0.20 eV, while the best on-top functional in our study is tPBE0, which achieves an MUE of 0.15 eV. This is three-quarters of the error of M06-SX and about half of the error of tPBE0’s KS-DFT counterpart PBE0 (MUE 0.29 eV for the intersecting subset), suggesting that MC-PDFT performance surpasses TD-DFT when MC-PDFT uses a well-chosen active space. Moreover, the performance of tPBE0 aligns closely with that of NEVPT2 (MUE 0.14 eV on the intersecting subset), suggesting that equally high accuracy can be obtained at lower cost by using MC-PDFT.

V. CONCLUSION

We derived the analytic nuclear gradients of SS-MC-PDFT and SA-MC-PDFT (with and without density fitting) for meta-GA and hybrid meta-GA on-top functionals. We verified our implementation by showing the analytic and numerical gradients for LiH agree to better than 1×10^{-5} hartree/bohr. Then we showed the utility of such nuclear gradients by performing geometry optimizations for the ground state and first excited singlet state of *s-trans*-butadiene and benzophenone. Because the derivation of the MC-PDFT nuclear gradients for

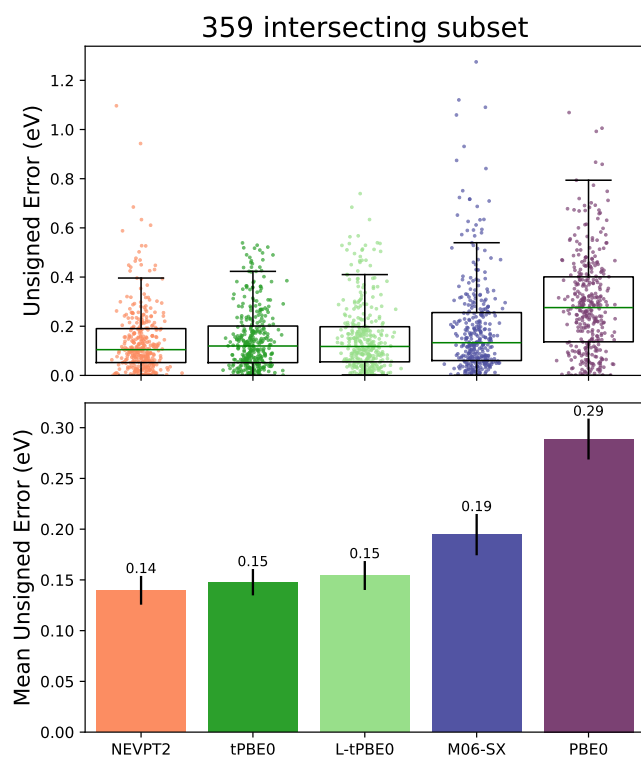


FIG. 3. Error statistics comparison between Liang *et al.*⁷⁵ and our study across the intersecting subset of 359 excitations. Results are shown for NEVPT2, tPBE0, and L-tPBE0 from our study as well as the M06-SX and PBE0 KS-DFT functionals.

meta-GA on-top functionals produced the one-electron and two-electron on-top potentials for a meta-GA, it also enabled us to calculate L-PDFT energies with meta-GA on-top functionals. We used this capability to benchmark seven meta-GA on-top functionals and two hybrid meta-GA on-top functionals on the QUEST dataset of vertical excitation energies, and we found that the MC23 meta-GA functional performed the best of these nine functionals and is on par with the hybrid GA functional tPBE0.

A next step is to enable L-PDFT analytic nuclear gradients with a meta-GA on-top functional. This requires taking another derivative of the non-linear translation scheme.

SUPPLEMENTARY MATERIAL

Detailed analysis of numerical versus analytical gradients. Vertical excitation energy for each method and system within the QUESTDB (csv file). Plots of vertical excitation benchmarking for full QUEST dataset as well as L-tPBE0 thresholded systems and 359-excitation overlap subset with prior TD-DFT calculations; the 359 excitations used to compare TD-DFT and MC-PDFT; optimized *s-trans*-butadiene and benzophenol coordinates with total energies.

ACKNOWLEDGMENTS

This work was supported in part by the Air Force Office Scientific Research (grant no. FA9550-20-1-0360). M. R. Hennefarth acknowledges support by the National Science Foundation Graduate Research Fellowship under Grant No. 2140001. We also acknowledge the University of Chicago’s Research Computing Center for their support of this work. Any opinion, findings, and conclusions or recommendations expressed in this material are those of the author(s) and do not necessarily reflect the views of the National Science Foundation.

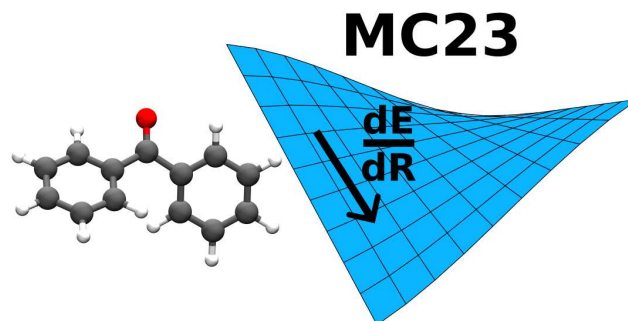
REFERENCES

- [1] W. Kohn and L. J. Sham, *Phys. Rev.* **140**, A1133 (1965).
- [2] B. O. Roos, P. R. Taylor, and P. E. M. Siegbahn, *Chem. Phys.* **48**, 157 (1980).
- [3] B. O. Roos, in *Ab Initio Methods in Quantum Chemistry Part II*, Advances in Chemical Physics, Vol. 69, edited by K. P. Lawley (John Wiley & Sons, Ltd, Great Britain, 1987) pp. 399–445.
- [4] K. Ruedenberg, L. M. Cheung, and S. T. Elbert, *Int. J. Quantum Chem.* **16**, 1069 (1979).
- [5] M. R. Hermes and L. Gagliardi, *J. Chem. Theory Comput.* **15**, 972 (2019).
- [6] M. R. Hermes, R. Pandharkar, and L. Gagliardi, *J. Chem. Theory Comput.* **16**, 4923 (2020).
- [7] K. Andersson, P.-Å. Malmqvist, B. O. Roos, A. J. Sadlej, and Krzysztof Wolinski, *J. Phys. Chem.* **94**, 5483 (1990).
- [8] K. Andersson, P.-Å. Malmqvist, and B. O. Roos, *J. Chem. Phys.* **96**, 1218 (1992).
- [9] C. Angeli, R. Cimraglia, S. Evangelisti, T. Leininger, and J.-P. Malrieu, *J. Chem. Phys.* **114**, 10252 (2001).
- [10] G. Li Manni, R. K. Carlson, S. Luo, D. Ma, J. Olsen, D. G. Truhlar, and L. Gagliardi, *J. Chem. Theory Comput.* **10**, 3669 (2014).
- [11] P.-Å. Malmqvist, A. Rendell, and B. O. Roos, *J. Phys. Chem.* **94**, 5477 (1990).
- [12] C. Zhou, L. Gagliardi, and D. G. Truhlar, *J. Phys. Chem. A* **123**, 3389 (2019).
- [13] S. Odoh, G. Li Manni, R. K. Carlson, D. G. Truhlar, and L. Gagliardi, *Chem. Sci.* **7**, 3669 (2016).
- [14] R. Pandharkar, M. R. Hermes, C. J. Cramer, D. G. Truhlar, and L. Gagliardi, *J. Chem. Theory Comput.* **17**, 2843 (2021).
- [15] C. E. Hoyer, S. Ghosh, D. G. Truhlar, and L. Gagliardi, *J. Phys. Chem. Lett.* **7**, 586 (2016).
- [16] D. S. King, M. R. Hermes, D. G. Truhlar, and L. Gagliardi, *J. Chem. Theory Comput.* **18**, 6065 (2022).
- [17] P. B. Calio, D. G. Truhlar, and L. Gagliardi, *J. Chem. Theory Comput.* **18**, 614 (2022).
- [18] M. R. Hennefarth, D. G. Truhlar, and L. Gagliardi, *J. Chem. Theory Comput.* **20**, 8741 (2024).
- [19] R. K. Carlson, D. G. Truhlar, and L. Gagliardi, *J. Chem. Theory Comput.* **11**, 4077 (2015).
- [20] J. J. Bao, D. Zhang, S. Zhang, L. Gagliardi, and D. G. Truhlar, *Proc. Natl. Acad. Sci.* **122**, e2419413121 (2025).
- [21] R. Pandharkar, M. R. Hermes, D. G. Truhlar, and L. Gagliardi, *J. Phys. Chem. Lett.* **11**, 10158 (2020).

- [22] M. R. Hennefarth, M. R. Hermes, D. G. Truhlar, and L. Gagliardi, *J. Chem. Theory Comput.* **19**, 3172 (2023).
- [23] P.-F. Loos, M. Boggio-Pasqua, A. Scemama, M. Caffarel, and D. Jacquemin, *J. Chem. Theory Comput.* **15**, 1939 (2019).
- [24] P.-F. Loos, A. Scemama, A. Blondel, Y. Garniron, M. Caffarel, and D. Jacquemin, *J. Chem. Theory Comput.* **14**, 4360 (2018).
- [25] P.-F. Loos, F. Lipparini, M. Boggio-Pasqua, A. Scemama, and D. Jacquemin, *J. Chem. Theory Comput.* **16**, 1711 (2020).
- [26] P.-F. Loos, A. Scemama, M. Boggio-Pasqua, and D. Jacquemin, *J. Chem. Theory Comput.* **16**, 3720 (2020).
- [27] M. V eril, A. Scemama, M. Caffarel, F. Lipparini, M. Boggio-Pasqua, D. Jacquemin, and P.-F. Loos, *WIREs Comput. Mol. Sci.* **11**, e1517 (2021).
- [28] P.-F. Loos, A. Scemama, and D. Jacquemin, *J. Phys. Chem. Lett.* **11**, 2374 (2020).
- [29] T. Helgaker, P. J orgensen, and J. Olsen, *Molecular Electronic-Structure Theory* (John Wiley & Sons, Chichester, UK, 2000, pp. 36-37).
- [30] A. M. Sand, C. E. Hoyer, K. Sharkas, K. M. Kidder, R. Lindh, D. G. Truhlar, and L. Gagliardi, *J. Chem. Theory Comput.* **14**, 126 (2018).
- [31] T. R. Scott, M. R. Hermes, A. M. Sand, M. S. Oakley, D. G. Truhlar, and L. Gagliardi, *J. Chem. Phys.* **153**, 014106 (2020).
- [32] W. H. Press, S. A. Teukolsky, W. T. Vetterling, and B. P. Flannery, *Numerical Recipes in Fortran 77: The Art of Scientific Computing*, 2nd ed. (Cambridge University Press, Cambridge, UK, 1992).
- [33] A. Bernhardtsson, R. Lindh, J. Olsen, and M. Fulscher, *Mol. Phys.* **96**, 617 (1999).
- [34] C. W. Misner, K. S. Thorne, and J. A. Wheeler, *Gravitation* (Macmillan, San Francisco, CA, USA, 1973).
- [35] N. H. F. Beebe and J. Linderberg, *Int. J. Quantum Chem.* **12**, 683 (1977).
- [36] T. R. Scott, M. S. Oakley, M. R. Hermes, A. M. Sand, R. Lindh, D. G. Truhlar, and L. Gagliardi, *J. Chem. Phys.* **154**, 074108 (2021).
- [37] Q. Sun, T. C. Berkelbach, N. S. Blunt, G. H. Booth, S. Guo, Z. Li, J. Liu, J. D. McClain, E. R. Sayfutyarova, S. Sharma, S. Wouters, and G. K.-L. Chan, *WIREs Comput. Mol. Sci.* **8**, e1340 (2018).
- [38] Q. Sun, X. Zhang, S. Banerjee, P. Bao, M. Barbry, N. S. Blunt, N. A. Bogdanov, G. H. Booth, J. Chen, Z.-H. Cui, J. J. Eriksen, Y. Gao, S. Guo, J. Hermann, M. R. Hermes, K. Koh, P. Koval, S. Lehtola, Z. Li, J. Liu, N. Mardirossian, J. D. McClain, M. Motta, B. Mussard, H. Q. Pham, A. Pulkin, W. Purwanto, P. J. Robinson, E. Ronca, E. R. Sayfutyarova, M. Scheurer, H. F. Schurkus, J. E. T. Smith, C. Sun, S.-N. Sun, S. Upadhyay, L. K. Wagner, X. Wang, A. White, J. D. Whitfield, M. J. Williamson, S. Wouters, J. Yang, J. M. Yu, T. Zhu, T. C. Berkelbach, S. Sharma, A. Y. Sokolov, and G. K.-L. Chan, *J. Chem. Phys.* **153**, 024109 (2020).
- [39] PySCF-forge (2025).
- [40] Q. Sun, *J. Comput. Chem.* **36**, 1664 (2015).
- [41] M. A. L. Marques, M. J. T. Oliveira, and T. Burnus, *Comput. Phys. Commun.* **183**, 2272 (2012).
- [42] S. Lehtola, C. Steigemann, M. J. T. Oliveira, and M. A. L. Marques, *SoftwareX* **7**, 1 (2018).
- [43] T. H. Dunning Jr., *J. Chem. Phys.* **90**, 1007 (1989).
- [44] R. A. Kendall, T. H. Dunning Jr., and R. J. Harrison, *J. Chem. Phys.* **96**, 6796 (1992).
- [45] M. R. Hermes, *mrh* (2025).
- [46] L.-P. Wang and C. Song, *J. Chem. Phys.* **144**, 214108 (2016).
- [47] D. Feller, *J. Comput. Chem.* **17**, 1571 (1996).
- [48] K. L. Schuchardt, B. T. Didier, T. Elsethagen, L. Sun, V. Gurumoorthi, J. Chase, J. Li, and T. L. Windus, *J. Chem. Inf. Model.* **47**, 1045 (2007).
- [49] E. Papajak and D. G. Truhlar, *J. Chem. Theory Comput.* **7**, 10 (2010).
- [50] J. Tao, J. P. Perdew, V. N. Staroverov, and G. E. Scuseria, *Phys. Rev. Lett.* **91**, 146401 (2003).
- [51] J. P. Perdew, J. Tao, V. N. Staroverov, and G. E. Scuseria, *J. Chem. Phys.* **120**, 6898 (2004).
- [52] V. N. Staroverov, G. E. Scuseria, J. Tao, and J. P. Perdew, *J. Chem. Phys.* **119**, 12129 (2003).
- [53] J. Sun, A. Ruzsinszky, and J. P. Perdew, *Phys. Rev. Lett.* **115**, 036402 (2015).
- [54] J. W. Furness, A. D. Kaplan, J. Ning, J. P. Perdew, and J. Sun, *J. Phys. Chem. Lett.* **11**, 8208 (2020).
- [55] J. W. Furness, A. D. Kaplan, J. Ning, J. P. Perdew, and J. Sun, *J. Phys. Chem. Lett.* **11**, 9248 (2020).
- [56] Y. Zhao and D. G. Truhlar, *J. Chem. Phys.* **125**, 194101 (2006).
- [57] Y. Wang, X. Jin, H. S. Yu, D. G. Truhlar, and X. He, *Proc. Natl. Acad. Sci.* **114**, 8487 (2017).
- [58] H. S. Yu, X. He, and D. G. Truhlar, *J. Chem. Theory Comput.* **12**, 1280 (2016).
- [59] A. D. Boese and N. C. Handy, *J. Chem. Phys.* **116**, 9559 (2002).
- [60] D. S. King and L. Gagliardi, *J. Chem. Theory Comput.* **17**, 2817 (2021).
- [61] J. J. Bao, M. R. Hermes, T. R. Scott, A. M. Sand, R. Lindh, L. Gagliardi, and D. G. Truhlar, *Mol. Phys.* **120**, e2110534 (2022).
- [62] M. R. Hennefarth, M. R. Hermes, D. G. Truhlar, and L. Gagliardi, *J. Chem. Theory Comput.* **20**, 3637 (2024).
- [63] Y. Shu and D. G. Truhlar, *J. Am. Chem. Soc.* **139**, 13770 (2017).
- [64] W. Haugen, M. Tr etteberg, F. Kaufmann, K. Motzfeldt, D. H. Williams, E. Bunnenberg, C. Djerassi, and R. Records, *Acta Chem. Scand.* **20**, 1726 (1966).
- [65] M. A. Watson and G. K.-L. Chan, *J. Chem. Theory Comput.* **8**, 4013 (2012).
- [66] S. Aloise, C. Ruckebusch, L. Blanchet, J. R ehault, G. Buntinx, and J.-P. Huvenne, *J. Phys. Chem. A* **112**, 224 (2008).
- [67] R. Katoh, M. Kotani, Y. Hirata, and T. Okada, *Chem. Phys. Lett.* **264**, 631 (1997).
- [68] N. Ohmori, T. Suzuki, and M. Ito, *J. Phys. Chem.* **92**, 1086 (1988).
- [69] R. Hoffmann and J. R. Swenson, *J. Phys. Chem.* **74**, 415 (1970).
- [70] D.-C. Sergentu, R. Maurice, R. W. A. Havenith, R. Broer, and D. Roca-Sanju an, *Phys. Chem. Chem. Phys.* **16**, 25393 (2014).
- [71] B. Vlaisavljevich and T. Shiozaki, *J. Chem. Theory Comput.* **12**, 3781 (2016).
- [72] E. B. Fleischer, N. Sung, and S. Hawkinson, *J. Phys. Chem.* **72**, 4311 (1968).
- [73] T. Itoh, *J. Phys. Chem.* **89**, 3949 (1985).
- [74] M. R. Hennefarth, D. S. King, and L. Gagliardi, *J. Chem. Theory Comput.* **19**, 7983 (2023).

- [75] J. Liang, X. Feng, D. Hait, and M. Head-Gordon, *J. Chem. Theory Comput.* **18**, 3460 (2022).
- [76] Y. Wang, P. Verma, L. Zhang, Y. Li, Z. Liu, D. G. Truhlar, and X. He, *Proc. Natl. Acad. Sci.* **117**, 2294 (2020).

TOC GRAPHIC



Supporting Information: MC-PDFT Nuclear Gradients and L-PDFT Energies with Meta and Hybrid Meta On-Top Functionals for Ground- and Excited-State Geometry Optimization and Vertical Excitation Energies

Matthew R. Hennefarth,¹ Younghwan Kim,¹ Bhavnesh Jangid,¹ Jacob Wardzala,¹
Matthew R. Hermes,¹ Donald G. Truhlar,^{2,*} and Laura Gagliardi^{1,3,*}

¹*Department of Chemistry and Chicago Center for Theoretical Chemistry, University of Chicago, Chicago, IL 60637, USA*

²*Department of Chemistry, Chemical Theory Center, and Minnesota Supercomputing Institute, University of Minnesota, Minneapolis, MN 55455-0431, USA*

³*Pritzker School of Molecular Engineering, University of Chicago, Chicago, IL 60637, USA*

(Dated: July 17, 2025)

CONTENTS

SI. Validation of Analytical Gradients	S1
SII. Supporting Figures	S6
SIII. TD-DFT Excitations	S8
SIV. Optimized Geometries	S12
A. <i>s-trans</i> -butadiene	S12
B. Benzophenone	S13

SI. VALIDATION OF ANALYTICAL GRADIENTS

We define the unsigned error (UE) and unsigned relative error (URE) for the nuclear gradients as

$$\text{UE} = |\text{Analytic} - \text{Numerical}| \quad (\text{S1})$$

$$\text{URE} = \left| \frac{\text{Analytic} - \text{Numerical}}{\text{Numerical}} \right| \quad (\text{S2})$$

The common log of the UE and URE for the nuclear gradient of the ground state of LiH scanned between 0.5 Å to 4.0 Å with a step size of 0.1 Å using SS-MC-PDFT with tPBE0 (a hybrid GA on-top functional) and MC23 (a hybrid meta-GA on-top functional) is shown in fig. S1. This figure shows that the UE is stable at all bond distances. We show histograms of the errors in fig. S2. This figure shows that UE is below 1×10^{-4} hartree/bohr with the majority being on the order of 1×10^{-6} hartree/bohr (fig. S2). The URE tends to grow as the bond distance increases because the potential energy curve becomes flatter, but it never goes above 1×10^{-2} .

Figure S3 shows the common log of the UE and URE for the nuclear gradients of the ground and first singlet excited state of LiH using SA-MC-PDFT. Both the UE and URE are stable with respect to the bond length, with the URE for both states increasing as the bond length increases due to the potential energy curves flattening out. Again, the errors are normally distributed and the histograms are shown in fig. S4. All UE are below 1×10^{-4} hartree/bohr with the majority being on the order of 1×10^{-6} hartree/bohr. The URE are slightly higher with the majority being on the order of 1×10^{-4} .

* corresponding author: truhlar@umn.edu

* corresponding author: lgagliardi@uchicago.edu

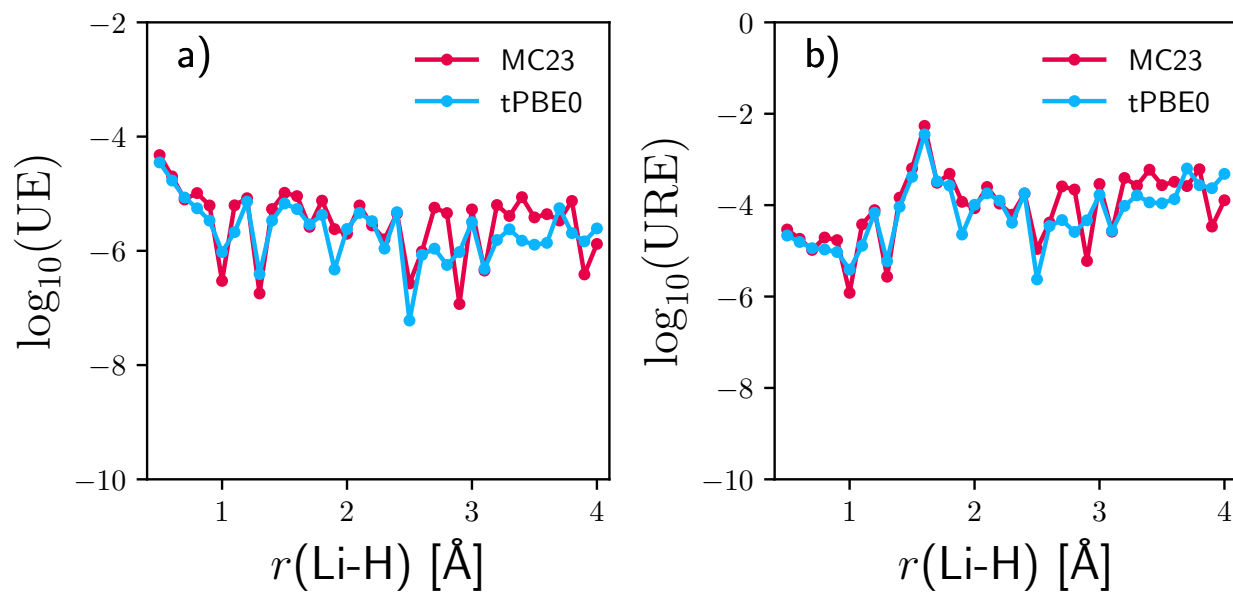


FIG. S1. Common log of the UE in atomic units (a) and URE (b) of the analytic gradients relative to the numerical gradients for the ground state of LiH using a SS-CASSCF reference wave function.

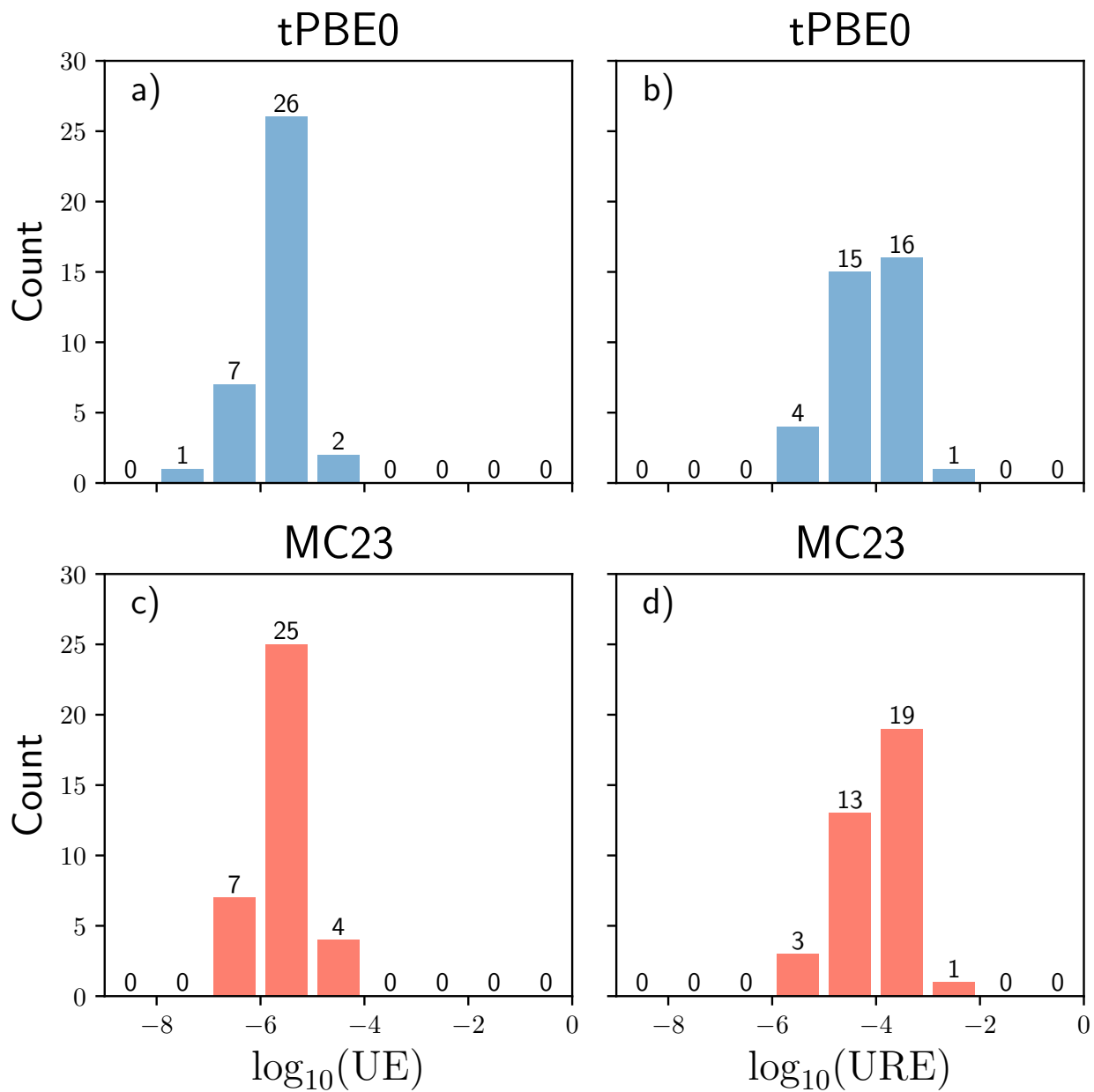


FIG. S2. Distribution of the common log of the UE in atomic units (a,c) and URE (b,d) of the analytic gradients relative to the numerical gradients for the ground state of LiH using a SS-CASSCF reference wave function. The top row (a,b) uses the tPBE0 function, and the bottom row (c,d) uses the MC23 functional.

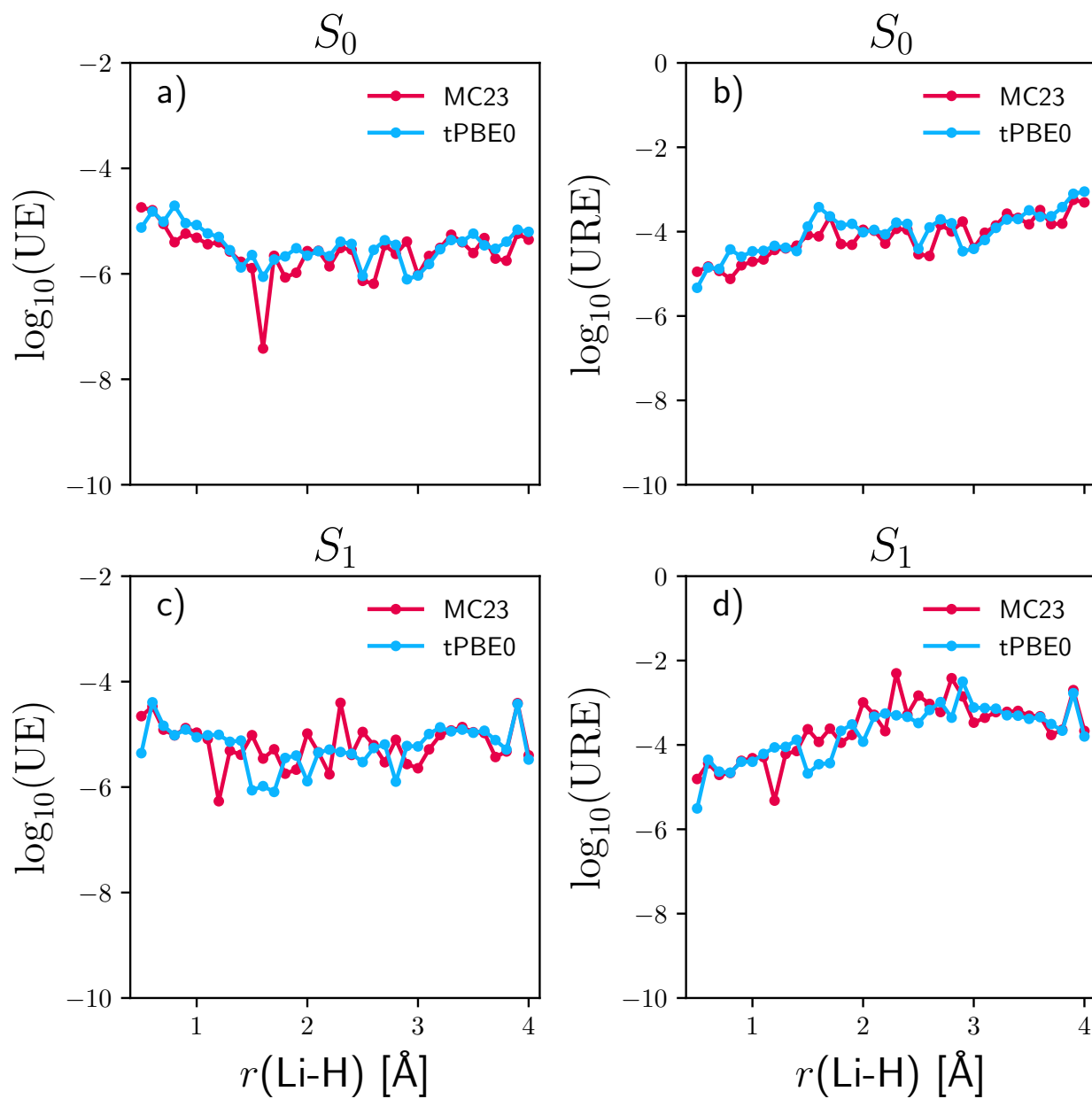


FIG. S3. Common log of the UE in atomic units (a,c) and URE (b,d) of the analytic gradients relative to the numerical gradients for the ground (a,b) and first excited (c,d) state of LiH using a SA-CASSCF reference wave function.

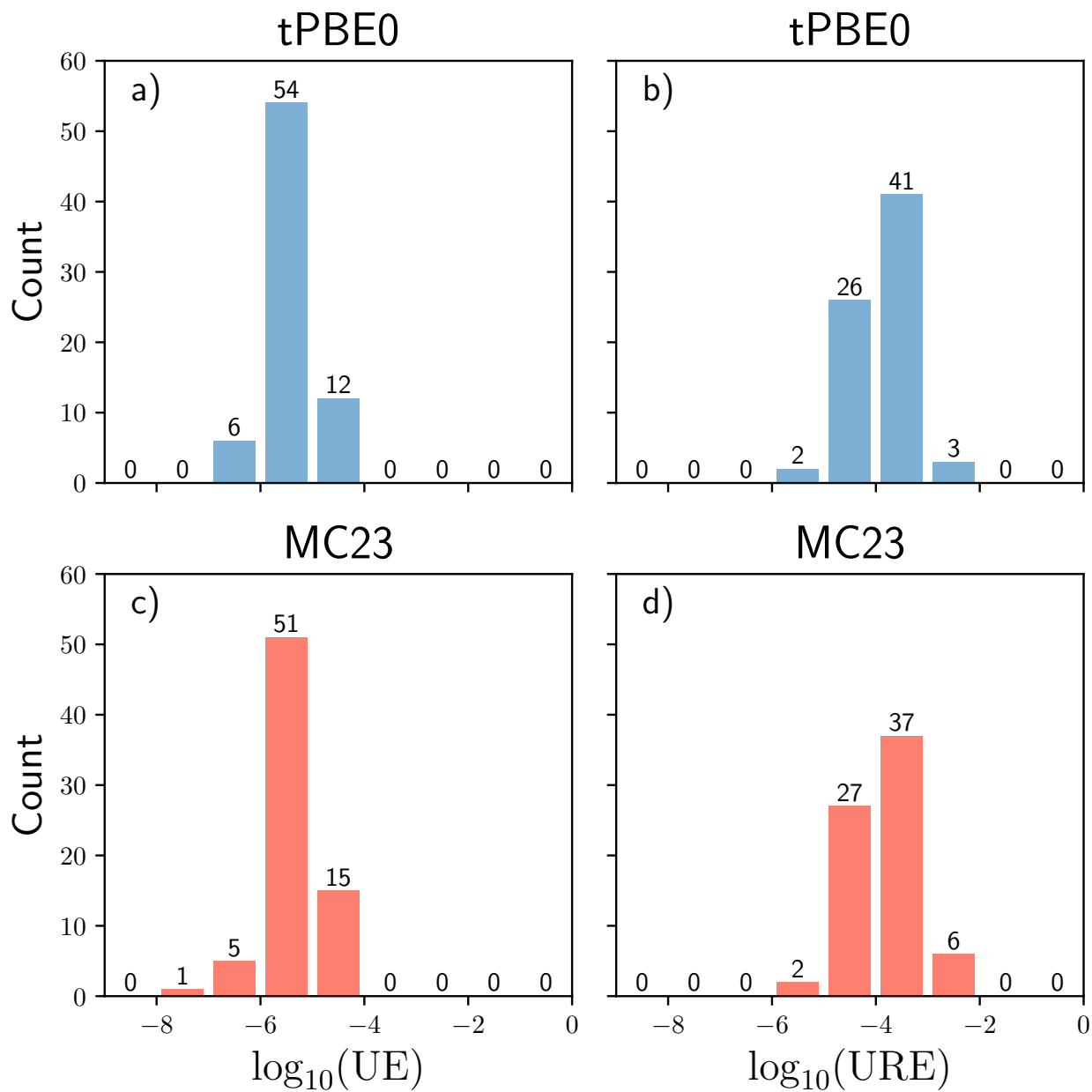


FIG. S4. Distribution of the common log of the UE (a,c) and URE (b,d) of the analytic gradients relative to the numerical gradients for the ground state of LiH using a SA-CASSCF reference wave function. The top row (a,b) uses the tPBE0 function, and the bottom row (c,d) uses the MC23 functional.

SII. SUPPORTING FIGURES

All data: 540 Excitations

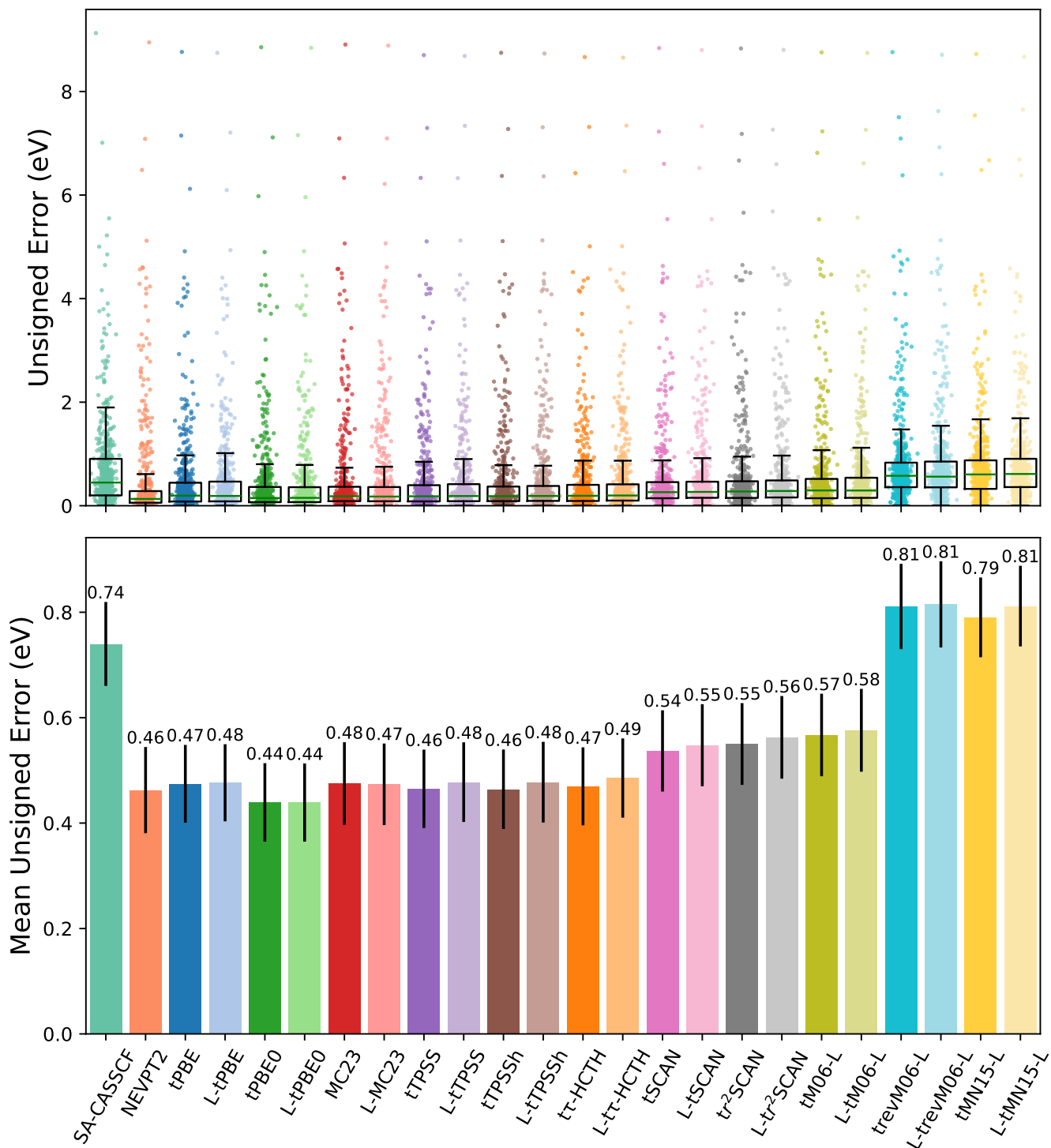


FIG. S5. Top: distribution of vertical excitation unsigned error and box and whisker plots over all 540 QUESTDB excitations for SA-CASSCF, NEVPT2, and 11 functionals for MC-PDFT and L-PDFT. Each dot represents a single unsigned error for the given method. The box represents the inter-quartile range and the horizontal green lines within each box indicates the median value. The whiskers extend $1.5\times$ the inter-quartile range. Bottom: bar plots of the mean unsigned error for each method on the 540 excitations with the black vertical lines indicating the 95% confidence intervals.

L-tPBE0 cutoff 0.55 eV: 444 Excitations

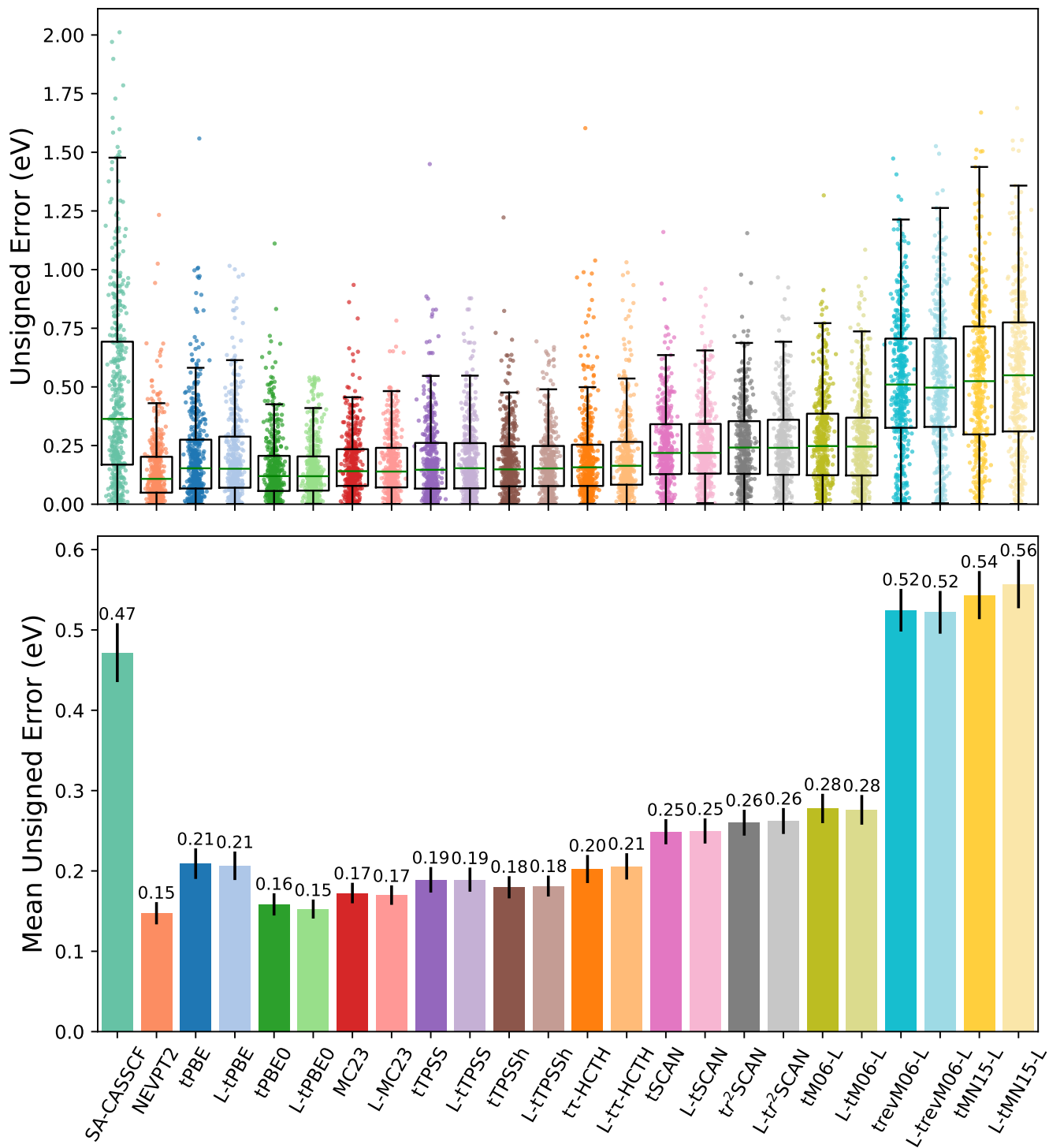


FIG. S6. Top: distribution of vertical excitation unsigned error and box and whisker plots over 444 excitations with an L-tPBE0 error cutoff of 0.55 eV for SA-CASSCF, NEVPT2, and 11 functionals for MC-PDFT and L-PDFT. Each dot represents a single unsigned error for the given method. The box represents the inter-quartile range and the horizontal green lines within each box indicates the median value. The whiskers extend $1.5\times$ the inter-quartile range. Bottom: bar plots of the mean unsigned error for each method on the 44 excitations with the black vertical lines indicating the 95 % confidence intervals.

SIII. TD-DFT EXCITATIONS

Here, we list the 359-excitations subset from the QUESTDB used to compare TD-DFT and MC-PDFT results.

1. acetaldehyde-x1	56. cclf-x1
2. acetaldehyde-x2	57. cf2-x2
3. acetone-x1	58. ch3-x2
4. acetone-x3	59. ch3-x3
5. acetone-x6	60. cn-x1
6. acetone-x7	61. cn-x2
7. acetylene-x1	62. co+-x1
8. acetylene-x2	63. co+-x2
9. acetylene-x3	64. cyanoacetylene-x1
10. acetylene-x4	65. cyanoacetylene-x2
11. acetylene-x5	66. cyanoacetylene-x3
12. acrolein-x7	67. cyanoacetylene-x4
13. acrolein-x8	68. cyanoformaldehyde-x1
14. allyl-x1	69. cyanoformaldehyde-x2
15. allyl-x2	70. cyanoformaldehyde-x3
16. aza-naphthalene-x1	71. cyanoformaldehyde-x4
17. aza-naphthalene-x2	72. cyanogen-x1
18. aza-naphthalene-x3	73. cyanogen-x2
19. aza-naphthalene-x4	74. cyanogen-x3
20. aza-naphthalene-x9	75. cyclopentadiene-x2
21. bef-x1	76. cyclopentadiene-x3
22. bef-x2	77. cyclopentadiene-x5
23. beh-x1	78. cyclopentadiene-x7
24. beh-x2	79. cyclopentadiene-x8
25. benzene-x1	80. cyclopentadiene-x9
26. benzene-x2	81. cyclopentadiene-x10
27. benzene-x3	82. cyclopentadienethione-x1
28. benzene-x8	83. cyclopentadienethione-x2
29. benzene-x9	84. cyclopentadienethione-x4
30. benzene-x10	85. cyclopentadienethione-x6
31. benzoquinone-x1	86. cyclopentadienethione-x7
32. benzoquinone-x2	87. cyclopentadienethione-x8
33. benzoquinone-x11	88. cyclopentadienone-x1
34. benzoquinone-x12	89. cyclopentadienone-x2
35. benzoquinone-x13	90. cyclopentadienone-x6
36. benzoquinone-x14	91. cyclopentadienone-x7
37. bh2-x1	92. cyclopentadienone-x8
38. butadiene-x1	93. cyclopropene-x1
39. butadiene-x7	94. cyclopropene-x3
40. butadiene-x8	95. cyclopropene-x4
41. carbon-monoxide-x1	96. cyclopropenethione-x1
42. carbon-monoxide-x2	97. cyclopropenethione-x2
43. carbon-monoxide-x3	98. cyclopropenethione-x3
44. carbon-monoxide-x4	99. cyclopropenethione-x4
45. carbon-monoxide-x7	100. cyclopropenethione-x5
46. carbon-monoxide-x8	101. cyclopropenethione-x6
47. carbon-monoxide-x9	102. cyclopropenethione-x7
48. carbon-monoxide-x10	103. cyclopropenethione-x8
49. carbon-monoxide-x11	104. cyclopropenethione-x9
50. carbonylfluoride-x1	105. cyclopropenethione-x10
51. carbonylfluoride-x2	106. cyclopropenone-x1
52. ccl2-x1	107. cyclopropenone-x2
53. ccl2-x2	108. cyclopropenone-x3
54. ccl2-x3	109. cyclopropenone-x4
55. ccl2-x4	110. cyclopropenone-x5

111. cyclopropenone-x7
112. cyclopropenone-x8
113. cyclopropenone-x9
114. cyclopropenone-x10
115. cyclopropenone-x11
116. diacetylene-x1
117. diacetylene-x2
118. diacetylene-x3
119. diacetylene-x4
120. diazirine-x1
121. diazirine-x2
122. diazirine-x3
123. diazirine-x5
124. diazirine-x6
125. diazirine-x7
126. diazirine-x8
127. diazomethane-x1
128. diazomethane-x2
129. diazomethane-x3
130. diazomethane-x4
131. diazomethane-x5
132. diazomethane-x6
133. diazomethane-x7
134. difluorodiazirine-x1
135. difluorodiazirine-x2
136. difluorodiazirine-x3
137. difluorodiazirine-x4
138. difluorodiazirine-x5
139. difluorodiazirine-x6
140. dinitrogen-x1
141. dinitrogen-x2
142. dinitrogen-x3
143. dinitrogen-x5
144. dinitrogen-x8
145. dinitrogen-x9
146. dinitrogen-x10
147. dinitrogen-x11
148. ethylene-x1
149. ethylene-x3
150. ethylene-x5
151. ethylene-x6
152. ethylene-x7
153. f2bo-x1
154. f2bo-x2
155. f2bs-x1
156. f2bs-x2
157. formaldehyde-x1
158. formaldehyde-x2
159. formaldehyde-x4
160. formaldehyde-x7
161. formaldehyde-x9
162. formaldehyde-x10
163. formaldehyde-x11
164. formaldehyde-x13
165. formamide-x1
166. formamide-x5
167. formamide-x6
168. formylfluoride-x1
169. formylfluoride-x2
170. furan-x1
171. furan-x2
172. furan-x3
173. furan-x6
174. furan-x7
175. furan-x8
176. furan-x9
177. glyoxal-x1
178. glyoxal-x2
179. glyoxal-x4
180. glyoxal-x5
181. glyoxal-x6
182. glyoxal-x7
183. glyoxal-x8
184. glyoxal-x9
185. h2bo-x1
186. h2bo-x2
187. h2po-x1
188. h2po-x2
189. h2ps-x1
190. h2ps-x2
191. hccl-x1
192. hcf-x1
193. hco-x1
194. hcp-x1
195. hcp-x2
196. hcp-x3
197. hcp-x4
198. hexatriene-x1
199. hexatriene-x3
200. hexatriene-x4
201. hexatriene-x5
202. hexatriene-x6
203. hoc-x1
204. hpo-x1
205. hps-x1
206. hsif-x1
207. hydrogen-chloride-x1
208. hydrogen-sulfide-x1
209. hydrogen-sulfide-x2
210. hydrogen-sulfide-x3
211. hydrogen-sulfide-x4
212. imidazole-x1
213. imidazole-x2
214. imidazole-x3
215. imidazole-x5
216. imidazole-x6
217. imidazole-x7
218. imidazole-x8
219. isobutene-x2
220. isobutene-x3
221. ketene-x1
222. ketene-x2
223. ketene-x5
224. ketene-x6
225. ketene-x7
226. maleimide-x2

- 227. maleimide-x3
- 228. maleimide-x7
- 229. maleimide-x8
- 230. methanimine-x1
- 231. methanimine-x2
- 232. methylenecyclopropene-x1
- 233. methylenecyclopropene-x2
- 234. methylenecyclopropene-x3
- 235. methylenecyclopropene-x5
- 236. methylenecyclopropene-x6
- 237. naphthalene-x1
- 238. naphthalene-x2
- 239. naphthalene-x3
- 240. naphthalene-x4
- 241. nco-x1
- 242. nh2-x1
- 243. nitromethyl-x1
- 244. nitromethyl-x2
- 245. nitromethyl-x4
- 246. nitrosomethane-x1
- 247. nitrosomethane-x4
- 248. nitrosomethane-x5
- 249. octatetraene-x1
- 250. oh-x1
- 251. oh-x2
- 252. ph2-x1
- 253. propynal-x1
- 254. propynal-x2
- 255. propynal-x3
- 256. propynal-x4
- 257. pyrazine-x1
- 258. pyrazine-x2
- 259. pyrazine-x3
- 260. pyrazine-x4
- 261. pyrazine-x6
- 262. pyrazine-x7
- 263. pyrazine-x14
- 264. pyrazine-x15
- 265. pyrazine-x16
- 266. pyrazine-x17
- 267. pyrazine-x18
- 268. pyrazine-x19
- 269. pyridazine-x4
- 270. pyridazine-x6
- 271. pyridazine-x8
- 272. pyridazine-x9
- 273. pyridazine-x11
- 274. pyridine-x2
- 275. pyridine-x4
- 276. pyridine-x6
- 277. pyridine-x7
- 278. pyridine-x10
- 279. pyridine-x12
- 280. pyridine-x13
- 281. pyridine-x15
- 282. pyrimidine-x1
- 283. pyrimidine-x2
- 284. pyrimidine-x3
- 285. pyrimidine-x7
- 286. pyrimidine-x8
- 287. pyrimidine-x10
- 288. pyrimidine-x11
- 289. pyrrole-x1
- 290. pyrrole-x2
- 291. pyrrole-x3
- 292. pyrrole-x4
- 293. pyrrole-x5
- 294. pyrrole-x7
- 295. pyrrole-x8
- 296. pyrrole-x9
- 297. pyrrole-x10
- 298. sicl2-x1
- 299. sicl2-x2
- 300. silylidene-x1
- 301. silylidene-x2
- 302. streptocyanine-c1-x1
- 303. streptocyanine-c1-x2
- 304. streptocyanine-c3-x1
- 305. streptocyanine-c3-x2
- 306. streptocyanine-c5-x1
- 307. streptocyanine-c5-x2
- 308. tetrazine-x1
- 309. tetrazine-x2
- 310. tetrazine-x4
- 311. tetrazine-x5
- 312. tetrazine-x6
- 313. tetrazine-x7
- 314. tetrazine-x11
- 315. tetrazine-x12
- 316. tetrazine-x13
- 317. tetrazine-x15
- 318. tetrazine-x16
- 319. tetrazine-x17
- 320. thioacetone-x1
- 321. thioacetone-x2
- 322. thioacetone-x3
- 323. thioacetone-x6
- 324. thioacetone-x7
- 325. thioacrolein-x1
- 326. thioacrolein-x2
- 327. thioformaldehyde-x1
- 328. thioformaldehyde-x2
- 329. thioformaldehyde-x3
- 330. thioformaldehyde-x4
- 331. thioformaldehyde-x5
- 332. thioformaldehyde-x6
- 333. thiophene-x1
- 334. thiophene-x2
- 335. thiophene-x3
- 336. thiophene-x4
- 337. thiophene-x9
- 338. thiophene-x10
- 339. thiophene-x11
- 340. thiophene-x12
- 341. thiopropynal-x1
- 342. thiopropynal-x2

343. triazine-x1
 344. triazine-x2
 345. triazine-x3
 346. triazine-x4
 347. triazine-x5
 348. triazine-x9
 349. triazine-x10
 350. triazine-x11
 351. triazine-x12

TABLE S1. Mean unsigned error (MUE) on the 359-excitation subset for MC-PDFT, L-PDFT, SA-CASSCF, and NEVPT2.

Method	MUE
SA-CASSCF	0.47
NEVPT2	0.15
tPBE	0.15
L-tPBE	0.16
MC23	0.17
L-MC23	0.18
tTPSS	0.18
L-tTPSS	0.20
tTPSSh	0.18
L-tTPSSh	0.19
t τ -HCTH	0.20
L-t τ -HCTH	0.21
tSCAN	0.25
L-tSCAN	0.26
t r^2 SCAN	0.26
L-t r^2 SCAN	0.27
tM06-L	0.28
L-tM06-L	0.28
trevM06-L	0.53
L-trevM06-L	0.53
tMN15-L	0.54
L-tMN15-L	0.57

352. triazine-x13
 353. triazine-x14
 354. water-x1
 355. water-x2
 356. water-x3
 357. water-x4
 358. water-x5
 359. water-x6

TABLE S2. Mean unsigned error (MUE) on the 359-excitation subset for TD-DFT.

Method	MUE
M06-SX	0.20
ω B97X-D	0.20
BMK	0.20
ω B97X-V	0.21
SOGGA11-X	0.22
CAM-B3LYP	0.23
ω B97M-V	0.24
M06-2X	0.24
LRC- ω PBEh	0.25
LRC- ω PBE	0.25
MPW1K	0.27
rCAM-B3LYP	0.27
ω M05-D	0.28
PW6B95	0.28
MN15	0.28
PBE0	0.29
HSEHJS	0.29
BHHLYP	0.30
MPW1PW91	0.30
PBE50	0.32
M11	0.32
revTPSSh	0.33
MS2h	0.33
B3LYP	0.34
B97M-V	0.35
SCAN0	0.35
TPSSh	0.35
M06-L	0.36
mBEEF	0.38
MS2	0.39
MVSh	0.40
MVS	0.41
revTPSS	0.41
SCAN	0.41
revM06-L	0.44
TPSS	0.44
MN15-L	0.46
SPW92	0.48
B97-D	0.49
PBE	0.52
MPW91	0.53
BLYP	0.55
MN12-SX	0.57

SIV. OPTIMIZED GEOMETRIES

A. *s-trans*-butadieneTABLE S3. SA(2)-tPBE0(4,4)/jul-cc-pVTZ *s-trans*-butadiene equilibrium ground-state geometry (in Å). State 0 energy: -155.596 717 949 266 83 hartree. State 1 energy: -155.345 966 607 112 96 hartree

C	1.16562	0.00002	-1.43507
C	0.02921	-0.00001	-0.72863
C	-0.02921	0.00001	0.72863
C	-1.16562	-0.00002	1.43507
H	-0.92602	-0.00004	-1.25045
H	1.16140	0.00001	-2.51899
H	2.13583	0.00006	-0.94671
H	0.92602	0.00004	1.25045
H	-1.16140	-0.00001	2.51899
H	-2.13583	-0.00006	0.94671

TABLE S4. SA(2)-tPBE0(4,4)/jul-cc-pVTZ *s-trans*-butadiene equilibrium excited-state geometry (in Å). State 0 energy: -155.559 193 293 145 88 hartree. State 1 energy: -155.387 883 814 769 05 hartree

C	1.26724	0.00003	-1.51465
C	0.01136	-0.00001	-0.70085
C	-0.01136	0.00001	0.70085
C	-1.26724	-0.00003	1.51465
H	-0.93019	-0.00005	-1.24066
H	1.21966	0.00002	-2.59375
H	2.23497	0.00007	-1.03120
H	0.93019	0.00005	1.24066
H	-1.21966	-0.00002	2.59375
H	-2.23497	-0.00007	1.03120

TABLE S5. SA(2)-MC23(4,4)/jul-cc-pVTZ *s-trans*-butadiene equilibrium ground-state geometry (in Å). State 0 energy: -155.914 083 615 645 2 hartree. State 1 energy: -155.660 065 114 803 9 hartree

C	1.16001	0.00002	-1.42829
C	0.02498	-0.00001	-0.72515
C	-0.02498	0.00001	0.72515
C	-1.16001	-0.00002	1.42829
H	-0.92823	-0.00004	-1.24117
H	1.15729	0.00001	-2.50707
H	2.12204	0.00006	-0.93441
H	0.92823	0.00004	1.24117
H	-1.15729	-0.00001	2.50707
H	-2.12204	-0.00006	0.93441

TABLE S6. SA(2)-MC23(4,4)/jul-cc-pVTZ *s-trans*-butadiene equilibrium excited-state geometry (in Å). State 0 energy: -155.876 719 930 215 22 hartree. State 1 energy: -155.701 514 124 093 73 hartree

C	1.25900	0.00003	-1.50606
C	0.00591	-0.00001	-0.69834
C	-0.00591	0.00001	0.69834
C	-1.25900	-0.00003	1.50606
H	-0.93508	-0.00005	-1.22984
H	1.21518	0.00002	-2.58036
H	2.21847	0.00007	-1.01646
H	0.93508	0.00005	1.22984
H	-1.21518	-0.00002	2.58036
H	-2.21847	-0.00007	1.01646

B. Benzophenone

TABLE S7. SA(3)-CASSCF(8,7)/cc-pVDZ benzophenone equilibrium ground-state geometry (in Å). State 0 energy: -573.072 880 122 382 5 hartree. State 1 energy: -572.932 048 309 600 9 hartree. State 2 energy: -572.824 379 466 825 1 hartree.

C	-1.29538	0.17462	-0.29053
C	0.00000	0.00000	-1.02775
O	0.00000	0.00000	-2.24119
C	1.29538	-0.17462	-0.29053
C	2.48344	0.27072	-0.89098
C	3.70016	0.06434	-0.27776
C	3.76928	-0.61470	0.93765
C	2.60328	-1.08117	1.53019
C	1.37771	-0.86208	0.92676
H	2.42993	0.77885	-1.84269
H	4.60605	0.42680	-0.74542
H	4.72607	-0.78074	1.41426
H	2.65020	-1.61945	2.46759
H	0.47962	-1.23706	1.39712
C	-1.37771	0.86208	0.92676
C	-2.60328	1.08117	1.53019
C	-3.76928	0.61470	0.93765
C	-3.70016	-0.06434	-0.27776
C	-2.48344	-0.27072	-0.89098
H	-0.47962	1.23706	1.39712
H	-2.65020	1.61945	2.46759
H	-4.72607	0.78074	1.41426
H	-4.60605	-0.42680	-0.74542
H	-2.42993	-0.77885	-1.84269

TABLE S8. SA(3)-CASSCF(8,7)/cc-pVDZ benzophenone equilibrium excited-state geometry (in Å). State 0 energy: -573.042 193 181 727 hartree. State 1 energy: -572.961 031 720 203 9 hartree. State 2 energy: -572.853 414 757 668 9 hartree.

C	-1.30158	0.18026	-0.21882
C	0.00000	0.00000	-0.81881
O	0.00000	0.00000	-2.18749
C	1.30158	-0.18026	-0.21882
C	2.46513	0.07964	-0.98306
C	3.72024	-0.10131	-0.44767
C	3.87605	-0.55061	0.86096
C	2.74157	-0.83021	1.62239
C	1.48026	-0.65769	1.10099
H	2.36792	0.44165	-1.99667
H	4.59173	0.11369	-1.05201
H	4.86350	-0.68970	1.27889
H	2.85023	-1.20445	2.63194
H	0.62226	-0.92560	1.69794
C	-1.48026	0.65769	1.10099
C	-2.74157	0.83021	1.62239
C	-3.87605	0.55061	0.86096
C	-3.72024	0.10131	-0.44767
C	-2.46513	-0.07964	-0.98306
H	-0.62226	0.92560	1.69794
H	-2.85023	1.20445	2.63194
H	-4.86350	0.68970	1.27889
H	-4.59173	-0.11369	-1.05201
H	-2.36792	-0.44165	-1.99667

TABLE S9. SA(3)-tPBE(8,7)/cc-pVDZ benzophenone equilibrium ground-state geometry (in Å). State 0 energy: -575.834 130 302 756 4 hartree. State 1 energy: -575.695 276 141 585 5 hartree. State 2 energy: -575.619 243 738 847 6 hartree.

C	-1.29990	0.15853	-0.28478
C	0.00000	0.00000	-1.04518
O	0.00000	0.00000	-2.26270
C	1.29990	-0.15853	-0.28478
C	2.48761	0.25154	-0.91683
C	3.72485	0.04444	-0.30104
C	3.79189	-0.60995	0.93954
C	2.62869	-1.04756	1.56099
C	1.37635	-0.81554	0.95475
H	2.41811	0.72944	-1.90088
H	4.64507	0.38625	-0.79268
H	4.76690	-0.78097	1.41569
H	2.67730	-1.57058	2.52510
H	0.46172	-1.17093	1.44580
C	-1.37635	0.81554	0.95475
C	-2.62869	1.04756	1.56099
C	-3.79189	0.60995	0.93954
C	-3.72485	-0.04444	-0.30104
C	-2.48761	-0.25154	-0.91683
H	-0.46172	1.17093	1.44580
H	-2.67730	1.57058	2.52510
H	-4.76690	0.78097	1.41569
H	-4.64507	-0.38625	-0.79268
H	-2.41811	-0.72944	-1.90088

TABLE S10. SA(3)-tPBE(8,7)/cc-pVDZ benzophenone equilibrium excited-state geometry (in Å). State 0 energy: $-575.808\ 825\ 436\ 339\ 4$ hartree. State 1 energy: $-575.714\ 853\ 721\ 891\ 7$ hartree. State 2 energy: $-575.627\ 163\ 932\ 084\ 7$ hartree.

C	-1.29608	0.17524	-0.23399
C	0.00000	0.00000	-0.84513
O	0.00000	0.00000	-2.19778
C	1.29608	-0.17524	-0.23399
C	2.46851	0.07881	-1.00032
C	3.74024	-0.10561	-0.44380
C	3.88045	-0.54179	0.87418
C	2.73872	-0.81508	1.63686
C	1.45927	-0.64736	1.09835
H	2.37266	0.44910	-2.02901
H	4.62906	0.10467	-1.05360
H	4.87953	-0.67952	1.30808
H	2.84102	-1.18653	2.66533
H	0.58193	-0.92862	1.69111
C	-1.45927	0.64736	1.09835
C	-2.73872	0.81508	1.63686
C	-3.88045	0.54179	0.87418
C	-3.74024	0.10561	-0.44380
C	-2.46851	-0.07881	-1.00032
H	-0.58193	0.92862	1.69111
H	-2.84102	1.18653	2.66533
H	-4.87953	0.67952	1.30808
H	-4.62906	-0.10467	-1.05360
H	-2.37266	-0.44910	-2.02901

TABLE S11. SA(3)-tPBE0(8,7)/cc-pVDZ benzophenone equilibrium ground-state geometry (in Å). State 0 energy: $-575.142\ 951\ 025\ 225$ hartree. State 1 energy: $-575.003\ 915\ 259\ 807\ 4$ hartree. State 2 energy: $-574.919\ 640\ 297\ 206\ 6$ hartree.

C	-1.29831	0.16424	-0.28785
C	0.00000	0.00000	-1.04129
O	0.00000	0.00000	-2.25800
C	1.29831	-0.16424	-0.28785
C	2.48698	0.25666	-0.91006
C	3.71814	0.05022	-0.29329
C	3.78459	-0.61046	0.94019
C	2.61945	-1.05696	1.55229
C	1.37566	-0.83018	0.94544
H	2.42331	0.74411	-1.88505
H	4.63498	0.39823	-0.77750
H	4.75409	-0.77931	1.41811
H	2.66695	-1.58413	2.50937
H	0.46514	-1.19199	1.42971
C	-1.37566	0.83018	0.94544
C	-2.61945	1.05696	1.55229
C	-3.78459	0.61046	0.94019
C	-3.71814	-0.05022	-0.29329
C	-2.48698	-0.25666	-0.91006
H	-0.46514	1.19199	1.42971
H	-2.66695	1.58413	2.50937
H	-4.75409	0.77931	1.41811
H	-4.63498	-0.39823	-0.77750
H	-2.42331	-0.74411	-1.88505

TABLE S12. SA(3)-tPBE0(8,7)/cc-pVDZ benzophenone equilibrium excited-state geometry (in Å). State 0 energy: $-575.116\ 252\ 994\ 506\ 8$ hartree. State 1 energy: $-575.025\ 548\ 275\ 667\ 8$ hartree. State 2 energy: $-574.932\ 693\ 305\ 305\ 5$ hartree.

C	-1.29757	0.17657	-0.22909
C	0.00000	0.00000	-0.83679
O	0.00000	0.00000	-2.19431
C	1.29757	-0.17657	-0.22909
C	2.46727	0.07833	-0.99571
C	3.73482	-0.10536	-0.44566
C	3.88005	-0.54457	0.86966
C	2.74110	-0.81881	1.63299
C	1.46608	-0.64950	1.10010
H	2.37058	0.44562	-2.02063
H	4.61873	0.10568	-1.05465
H	4.87638	-0.68282	1.29852
H	2.84605	-1.19056	2.65651
H	0.59442	-0.92618	1.69522
C	-1.46608	0.64950	1.10010
C	-2.74110	0.81881	1.63299
C	-3.88005	0.54457	0.86966
C	-3.73482	0.10536	-0.44566
C	-2.46727	-0.07833	-0.99571
H	-0.59442	0.92618	1.69522
H	-2.84605	1.19056	2.65651
H	-4.87638	0.68282	1.29852
H	-4.61873	-0.10568	-1.05465
H	-2.37058	-0.44562	-2.02063

TABLE S13. SA(3)-MC23(8,7)/cc-pVDZ benzophenone equilibrium ground-state geometry (in Å). State 0 energy: $-576.243\ 750\ 252\ 499\ 9$ hartree. State 1 energy: $-576.103\ 190\ 380\ 728\ 6$ hartree. State 2 energy: $-576.016\ 513\ 943\ 189\ 2$ hartree.

C	-1.29027	0.15918	-0.28639
C	0.00000	0.00000	-1.03801
O	0.00000	0.00000	-2.25428
C	1.29027	-0.15918	-0.28639
C	2.47530	0.24157	-0.91835
C	3.70226	0.03871	-0.30140
C	3.76565	-0.59881	0.93963
C	2.60106	-1.02762	1.55981
C	1.36260	-0.80452	0.95381
H	2.40889	0.70946	-1.89837
H	4.61718	0.37067	-0.79067
H	4.73075	-0.76491	1.41753
H	2.64761	-1.53742	2.52136
H	0.45232	-1.15183	1.44092
C	-1.36260	0.80452	0.95381
C	-2.60106	1.02762	1.55981
C	-3.76565	0.59881	0.93963
C	-3.70226	-0.03871	-0.30140
C	-2.47530	-0.24157	-0.91835
H	-0.45232	1.15183	1.44092
H	-2.64761	1.53742	2.52136
H	-4.73075	0.76491	1.41753
H	-4.61718	-0.37067	-0.79067
H	-2.40889	-0.70946	-1.89837

TABLE S14. SA(3)-MC23(8,7)/cc-pVDZ benzophenone equilibrium excited-state geometry (in Å). State 0 energy: -576.216 907 236 755 6 hartree. State 1 energy: -576.125 067 045 286 1 hartree. State 2 energy: -576.029 743 926 020 3 hartree.

C	-1.29127	0.17395	-0.22531
C	0.00000	0.00000	-0.83141
O	0.00000	0.00000	-2.18623
C	1.29127	-0.17395	-0.22531
C	2.45454	0.07341	-0.99523
C	3.71834	-0.10777	-0.44705
C	3.86350	-0.53754	0.86768
C	2.72802	-0.80686	1.63195
C	1.45661	-0.63977	1.10192
H	2.35395	0.43276	-2.01873
H	4.59863	0.09716	-1.05557
H	4.85619	-0.67372	1.29477
H	2.83393	-1.17337	2.65262
H	0.58674	-0.91533	1.69349
C	-1.45661	0.63977	1.10192
C	-2.72802	0.80686	1.63195
C	-3.86350	0.53754	0.86768
C	-3.71834	0.10777	-0.44705
C	-2.45454	-0.07341	-0.99523
H	-0.58674	0.91533	1.69349
H	-2.83393	1.17337	2.65262
H	-4.85619	0.67372	1.29477
H	-4.59863	-0.09716	-1.05557
H	-2.35395	-0.43276	-2.01873